SCALING STUDY OF WAVE ROTOR TURBO-NORMALIZATION OF A SMALL INTERNAL COMBUSTION ENGINE

THESIS

Brandon D. Smith, Lieutenant, USN

AFIT/GAE/ENY/12-S48

DEPARTMENT OF THE AIR FORCE
AIR UNIVERSITY

AIR FORCE INSTITUTE OF TECHNOLOGY

Wright-Patterson Air Force Base, Ohio

SCALING STUDY OF WAVE ROTOR TURBO-NORMALIZATION OF A SMALL INTERNAL COMBUSTION ENGINE

THESIS

Presented to the Faculty

Department of Aeronautics and Astronautics

Graduate School of Engineering and Management

Air Force Institute of Technology

Air University

Air Education and Training Command

In Partial Fulfillment of the Requirements for the

Degree of Master of Science in Aeronautical Engineering

Brandon D. Smith, MS

Lieutenant, USN

September 2012

AFIT/GAE/ENY/12-S48

**SCALING STUDY OF WAVE ROTOR TURBO-NORMALIZATION OF A
SMALL INTERNAL COMBUSTION ENGINE**

Brandon D. Smith, MS

Lieutenant, USN

Approved:

_____   _____
Dr. Marcus Polanka (Chairman)   Date

_____   _____
Dr. Paul King (Member)   Date

_____   _____
Carl Hartsfield, Lt Col, USAF (Member)   Date

AFIT/GAE/ENY/12-S48

Abstract

One issue facing small Remotely Piloted Aircraft engines is their ability to maintain performance at altitude. Since many of these aircraft use commercial off the shelf engines originally designed for radio controlled aircraft and lawn care implements, the reduced pressure environment significantly degrades the operability of the engine as the altitude increases. An option to overcome this difficulty is to supercharge the system; however most superchargers are designed for larger, typically automotive, engines. As a supercharger's size is decreased, there are large efficiency losses. Therefore, there is a need to accomplish this function on a smaller scale without. One option is to utilize a device similar to the Comprex® wave rotor supercharger scaled for small engines. For this investigation, the author installed and evaluated the performance of a commercial Comprex® designed for a Mazda 626 2.0 liter diesel engine. The results were compared to simulation results from a one-dimensional computational fluid dynamics model. The loss models used by the code have been developed for and validated on wave machines designed for substantially higher corrected flow rates. Part of the current objective was to assess these scale related losses at a smaller scale. Results revealed a favorable comparison that demonstrates the loss models are applicable to the scale of the Comprex®. The computational fluid dynamics code's ability to simulate a wide range of wave rotor sizes indicated the code could be used on a pressure wave supercharger scaled to fit today's Remotely Piloted Aircraft engines to predict performance. The wave rotor code predicts the performance of the scaled pressure wave supercharger to be similar to

the full sized Comprex® providing approximately two times the ambient air pressure to

the engine inlet.

Acknowledgments

  I would like to express my sincere appreciation to my thesis advisor, Dr. Marc Polanka, for his guidance and support throughout the course of this thesis effort. Your insight and especially your patience were certainly appreciated. I would also like to thank my sponsor, Dr. Fred Schauer, for the opportunity to pursue and the funding to complete this research as well as the use of your facilities. Dr. Daniel Paxson was integral to my thesis completion. Thank you for taking the time to modify your code for my needs and always being available for questions. Without your wave rotor expertise this research would have never been possible. I cannot thank you enough.

  None my research would have been possible without the support and guidance of the entire D-Bay staff. Dr. John Hoke was instrumental in helping me make decisions on the rig building components and ensuring the facilities I required were available. Thank you to Dave Burris for creating and updating my LabVIEW code, Andy Naples for his knowledge and eagerness to help me at any time. Thank you to Chris Stevens, Rachel Russo, and Brian Sell for giving me advice and helping me throughout my research; without your help I would not have been able to complete this thesis.

  Without the assistance of the D-Bay lab technicians, none of this research would have been possible. I would like to thank Curt Rice for your help in the construction of my test rig and in running my experiments. I would also like to thank Justin Goffena for assisting in the construction of my test rig and being available at a moment's notice to make any parts I required.

Finally, I want to thank my wife and children for your support and understanding of the time required to be spent away from you for me to complete this research. Without your support I would not have been able to finish my thesis. I love you all.

Brandon D. Smith

Table of Contents

List of Figures

List of Tables

List of Symbols

A	Area
a	Speed of sound
A_{AO}	Area of AO port
A_{eff}	Effective area
A_{nom}	Nominal area
C_d	Discharge coefficient
C_p	Constant pressure specific heat
D	Engine displacement
g_c	Gravitational constant
h_l	Head loss
$h_{l,m}$	Minor head loss
K_e	Expansion loss coefficient
L	Length of rotor, length of pipe
L_e/D	Equivalent length
M	Mach number
$\dot{m}$	Mass flow rate
N	Engine speed
P_s	Static pressure
P_t	Total pressure
q	Heat transfer rate
R	Gas constant
r	Radius
t	Time for sonic wave to travel length of rotor
T	Time for one rotation of rotor
T_t	Total temperature
u	Velocity
$\dot{V}$	Volumetric flow rate
VE	Volumetric Efficiency
γ	Ratio of specific heats
ΔP	Change in pressure
ΔT	Change in temperature
ρ	Density

List of Abbreviations

ABB	Asea Brown Boveri
AC	Alternating current
AFIT	Air Force Institute of Technology
AFRL	Air Force Research Laboratory
AI	Air in port
AO	Air out port
BBC	Brown Boveri Company
cc	Cubic centimeters
CFD	Computational fluid dynamics
COTS	Commercial off the shelf
DC	Direct current
EI	Exhaust in port
EO	Exhaust out port
GRC	Glenn Research Center
HP	Horse power
ICE	Internal combustion engine
ICWR	Internal combustion wave rotor
ID	Inner diameter
IUPUI	Indiana University Purdue University of Indianapolis
MAF	Mass air flow
NASA	National Aeronautics and Space Administration
OD	Outer diameter
PWS	Pressure wave supercharger
RPA	Remotely piloted aircraft
RPM	Revolutions per minute

SCALING STUDY OF WAVE ROTOR TURBO-NORMALIZATION OF A SMALL INTERNAL COMBUSTION ENGINE

I. Introduction

I.1 General Issue

With the rapidly increasing use of remotely piloted aircraft (RPA) by today's military, the RPA manufacturers attempt to keep up with the demand while working within small acquisition budgets and quick timelines. In an attempt to meet these challenges, many chose to use commercial off the shelf (COTS) engines for the lower power UAVs. Often these engines were originally designed for powered lawn equipment or radio controlled aircraft since they are some of the few sources of engines with the appropriate power density for this scale aircraft. While these COTS engines are inexpensive and readily available, they were designed to operate at or near sea level. Previous research completed by Schmick (1) and Crosbie (2) show that these engines suffer performance and reliability degradation as the ambient pressure supplied to the engine is decreased. Since, in some applications, the RPA operational altitudes are in excess of 10,000 feet, they are continually operating at a decreased ambient pressure. This leads to issues with the performance and reliability that can affect critical missions.

There are many options available to alleviate the issues facing the use of COTS internal combustion engines to power small RPA. One option would be to design a new engine tailor made for the mission requirements of the RPA being constructed. While this would be the ideal choice for ensuring proper functionality of the engine, it would be very costly and time consuming. As mentioned previously, these small RPA are built on small budgets and require quick turnaround. These program requirements often preclude

this option and lead the current manufacturers to use COTS internal combustion engines to power these aircraft.

Since the use of COTS engines are the most cost and time effective choice as a power plant, a way must be found to make these engines retain the designed performance and reliability when operating at altitude. One option investigated by Crosbie (2) was to replace the typical engine carburetor with a fuel injection system. This option has shown to increase the reliability and allowed the engine to maintain sea level performance while operating at increased altitudes. The drawback of such a change is that it requires extensive modifications to the stock engine and requires a fuel map to be built for each operating altitude.

A second option for retaining the designed performance and reliability when operating in a decreased ambient pressure environment is to provide the engine inlet with sea level pressure air while operating at operational altitudes. This can be accomplished by turbo-normalizing the air supplied to the engine inlet. Turbo-normalization involves increasing the pressure of the ambient air at altitude to a pressure consistent with sea level air. This process is much like the use of a turbo or supercharger on an automobile to increase the sea level ambient air pressure to a greater pressure for increased engine performance. Turbo-normalization can be accomplished through the addition of a turbocharger, supercharger, or a pressure wave supercharger (PWS). The pressure wave super charger was chosen for this research due to its many advantages over the traditional turbo machinery choices. These advantages will be discussed in Chapter II.

I.2 Objectives

The ultimate goal of this research is to develop a pressure wave supercharger for use on an engine typical of those used in the small RPA currently employed by today's military. The 95cc Brison two-stroke engine was selected as the representative. To achieve this ultimate goal, four milestones had to be met. The four milestones are:

1. Characterization of a commercially used PWS through experimentation.

2. Simulation of the commercial PWS with a computational fluid dynamics (CFD) code to validate the code's ability to predict the PWS performance.

3. Design of a PWS scaled to fit the 95cc Brison engine.

4. Simulate the scaled PWS with the validated CFD code to predict the performance.

I.3 Methodology

Each of the four milestones leading to the ultimate objective of the development of a PWS scaled to fit a 95cc Brison engine required a different methodology. The methods used included experimentation, computational design, and simulation with CFD code.

For the first milestone of characterizing the commercially available PWS, a test rig was developed and built to simulate the Comprex® pressure wave supercharger's interaction with the engine. The Comprex® CX-93 used in the research was originally designed for use on a Mazda 626 2.0 liter diesel engine. Accurately simulating the engine's interaction with the Comprex® provided the performance information required to characterize the PWS. Simulation of the engine was accomplished by recreating the

pressure wave supercharger's two connections to the engine: the exhaust and the engine accessory drive. The exhaust was simulated with heated, compressed air and the accessory drive was replaced with an electric motor to drive the Comprex's® rotor. The Comprex® was then run at conditions (exhaust mass flow rates and engine speeds) consistent with the 2.0 liter engine operation. In preparation for the next milestone (CFD simulation), the total and static pressures, temperatures, and mass flows were recorded for each of the four ports of the Comprex®. These parameters were required for the experimental data collected to be compared with the predicted data from the simulation.

The completion of the second milestone required the use of a wave rotor code to simulate the Comprex® and predict its performance. The CFD code used was a quasi one-dimensional wave rotor computational fluid dynamics code developed by the NASA Glenn Research Center (GRC) in conjunction with their wave rotor studies. Using this code, the experimental conditions were simulated and the resulting predictions were compared with the pressures, temperatures and mass flow data collected from the experimental runs of the Comprex®. Good correlation between the experimental and simulated data indicated that the CFD code accurately predicted the flow conditions within the Comprex® and indicated that the CFD code could be used to simulate the scaled PWS and predict the performance.

The third milestone was to design a pressure wave supercharger scaled to fit the 95cc Brison engine. The size of the scaled PWS was found using the Brison's volumetric air flow requirements and equations published by Brown Boveri and Company, the developers of the Comprex®. The large reduction in size required some modification to the Comprex's® design to make it feasible to operate on the much smaller engine.

With the scaled pressure wave supercharger designed and the NASA GRC wave rotor code validated to accurately predict the performance of the Comprex®, the scaled PWS was simulated using the CFD code. The simulation provided information on the performance enhancement that could be expected with the addition of a PWS to the Brison engine.

II. Background and Previous Research

The overall objective of this research is to improve the performance and reliability of the two stroke internal combustions engines used in many of today's small remotely piloted vehicles. Since most of these engines are designed for use in radio controlled aircraft and lawn care implements, they were intended to be used at or near sea level. When these engines are used in remotely piloted aircraft, flown at operational altitudes in excess of 10,000 feet, the performance and reliability suffer. There are many ways to attempt to remedy this performance and reliability issue. For this research, the option of turbo-normalization of the inlet air was investigated. While many options are available for the turbo-normalization of these engines, the possibility of using a wave rotor pressure wave supercharger was chosen to be investigated for this research. The decision to pursue the pressure wave supercharger as a means of turbo-normalization led to researching what wave rotors are and how they work, the history of the development of wave rotors, the advantage of using wave rotors as opposed to other turbo machinery options for turbo-normalization and other wave rotor uses that have been and are currently being researched.

This section will focus on the basic premise behind and components of a wave rotor machine. It will also cover the early development and use of wave rotors beginning in the early 1900's, their rise to commercial success as a pressure wave supercharger (PWS), and research that has been completed and currently underway to exploit the advantages a wave rotor can bring to many systems. This section will also cover the design process and parameters needed to be considered in the design of a pressure wave supercharger. Though wave rotors have been used in a variety of applications, one has

not been developed to act as a pressure wave supercharger for an engine of the scale (95cc displacement) that is sought in this research.

II.1 What is a Wave Rotor

As described by Weber (3), traditionally, gas compression is achieved through either a piston and cylinder type device (reciprocating compressor) or by increasing the kinetic energy of the gas with rotating blades followed by a diffusion to a lower velocity and higher pressure (axial or centrifugal compressors). A wave rotor is an unsteady flow machine designed for performing inter-fluid pressure exchange more efficiently than conventional turbo-machinery devices.

The essential features of a wave rotor machine are a cylindrical drum with an array of channels arranged around the axis, as shown in Figure 1, with a stationary plate at each end. The endplates, shown in Figure 2, contain one or more ports to feed and exhaust the channels of the rotor with fluids, usually air and exhaust gases. The endplates are placed as close as possible to the rotor to prevent gas leakage while ensuring there is no rubbing between the components. The endplates are connected to each other with a cylinder. This connecting shroud, shown in Figure 3, is larger in diameter than the rotor and houses the rotor between the endplates. The rotor is kept in continuous rotation. This rotation allows for each cell of the rotor to periodically be exposed to the stationary ports of the endplates.
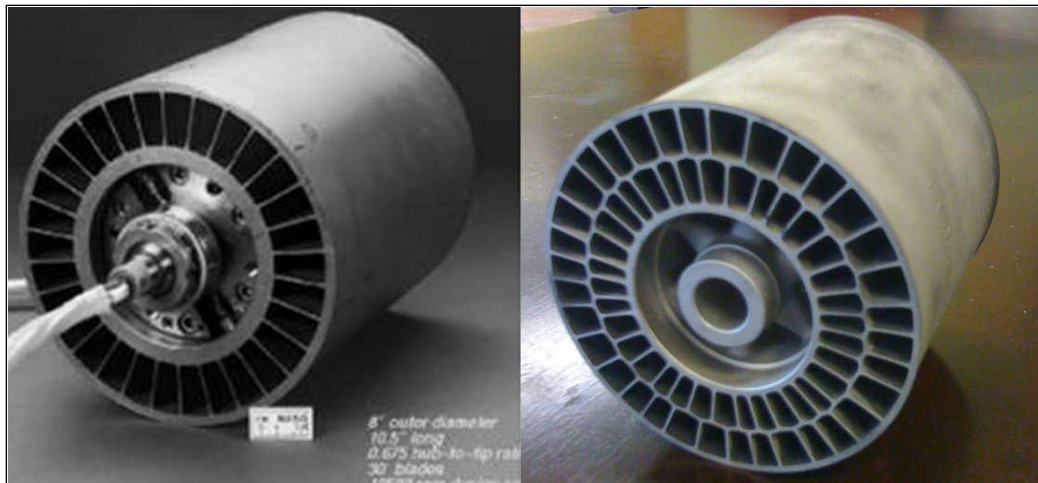
Figure 1: Rotor Examples

Figure 2: Endwall Examples

Figure 3: Endwalls connected by shroud

II.2 How a Wave Rotor Functions

A wave machine exploits the physical fact that when two fluids at different pressures are brought into direct contact, the fluids must equalize pressure before the fluids can mix. The fluids entering at each inlet ports are at different pressures (air at atmospheric pressure from the air inlet and exhaust gas at a pressure of around 3 atmospheres to the exhaust inlet). When the two fluids come into contact in the rotor cells, they equalize pressure before mixing can occur. This allows the air that entered the wave rotor at a pressure of one atmosphere and the exhaust gas that entered the cells at three atmospheres to equalize pressure so they are both at a pressure of approximately two atmospheres.

II.3 Development of pressure exchangers and pressure wave superchargers

Experimentation with pressure exchangers began in the early 20th century. The early experimenters included Knauff (4), Burghard (5), and Lebre (6). Knauff's original design in 1906 used a cellular drum rotating between endplates with multiple ports for the entrance and exit of gases at various pressures. The rotor contained curved blades and inclined stator nozzles to provide output shaft power. His design would come to be known as a pressure exchange engine (7). A second design by Knauff in 1906 and a design by Burghard in 1913, proposed a simpler device with long narrow passages for the pressure exchange to take place (7). This first pressure exchanger later became known as the Lebre machine because of his patent granted in 1928. Lebre's machine was a static pressure exchanger. In a static pressure exchanger the time for the wave (traveling at sonic velocity) to travel the length of the cell and back is much less than the time for the

9

cell to pass an endplate port (either inlet or outlet). This causes the wave effects to die out and the pressure in the cells to equalize with that in the port (8). Due to the slow rotation speed of the rotor in a static pressure exchanger, it is not able to take advantage of the pressure wave effects (both compression and expansion processes) essential to the dynamic pressure exchanger.

Akbari et al. (7) describe that the development of pressure wave propagation in unsteady flow to supercharge internal combustion engines (ICE) began in the 1940's by Brown Boveri Company (BBC), later Asea Brown Boveri (ABB) in Switzerland. BBC's first foray into wave rotors was using them as a topping stage for a 2200 horse power locomotive gas turbine. This first attempt showed satisfactory results, but design mismatch and integration problems left room for improvement. The upside of the turbine topping wave rotor was that it proved the concept of a wave machine. Iancu et al. (9) relate that though BBC originally envisioned their wave rotor machine as a topping stage for a locomotive turbine engine, BBC found its most success in the diesel engine industry as a pressure wave supercharger.

With a proof of concept, ITE Circuit Breaker Company and the U.S. Bureau of Aeronautics began working toward using a wave rotor to supercharge diesel engines. Between 1947 and 1955, ITE and the U.S. Bureau of Aeronautics manufactured and tested wave rotor superchargers on vehicle diesel engines. Success in this endeavor led to a cooperative program with BBC starting in 1955 (7). In 1956, the pressure wave supercharger, now with the trade name of Comprex®, was successfully introduced to the farm tractor market (10). In 1971, the first prototype was installed on a 290 horse power truck engine (11). In results from the more than 1400 miles of testing, the Comprex®

supercharged engine showed a higher average ground speed, lower average engine speed, and increased fuel economy when compared with the same truck engine with a traditional turbocharger over the same test regime (12). The Comprex® was first used on a passenger car in 1978 on an Opel 2.1 liter diesel engine (13). In 1987, Mazda made the first wide commercial use of the Comprex® by installing the supercharger on their 626 Capella. This resulted in 150,000 Comprex® supercharged diesel powered cars (7).

In 1998, Swissauto WENKO AG developed a Comprex® like supercharger, called the Hyprex, for use on gasoline engines and has shown success with a two-cylinder gasoline engine achieving low specific fuel consumption and emissions (14). The Hyprex® operates much like the Comprex®, except instead of the rotor being spun by the engine's accessory drive it is rotated with an electric motor controlled by the engine's Electric Control Unit (12). This allows for the rotor speed to be adjusted independently from the engine speed and the elimination of the endwall pockets as the rotor speed can be directly controlled and matched with the wave speed.

II.4 The Pressure Wave Supercharger

The Comprex® CX-93 used in this research is a pressure wave supercharger (PWS). The PWS consists of four main components: The rotor, the rotor shroud, and a hot and cold endwall. These components are shown in Figures 1-3. The PWS uses wave rotor technology to boost the pressure of the air exiting the machine much in the way that traditional superchargers and turbochargers are used. The main difference between the PWS and traditional turbo-machinery is the method used to achieve compression. While

11

turbo-machinery uses vanes and the associated aerodynamics to compress the air, the PWS uses gas dynamics as described above.

Heisler (15) describes the operation of a wave rotor supercharger (Figure 4) by dividing it into four phases: the cell compression phase, the cylinder filling phase, the cell exhaust gas expulsion phase, and the cell filling phase.
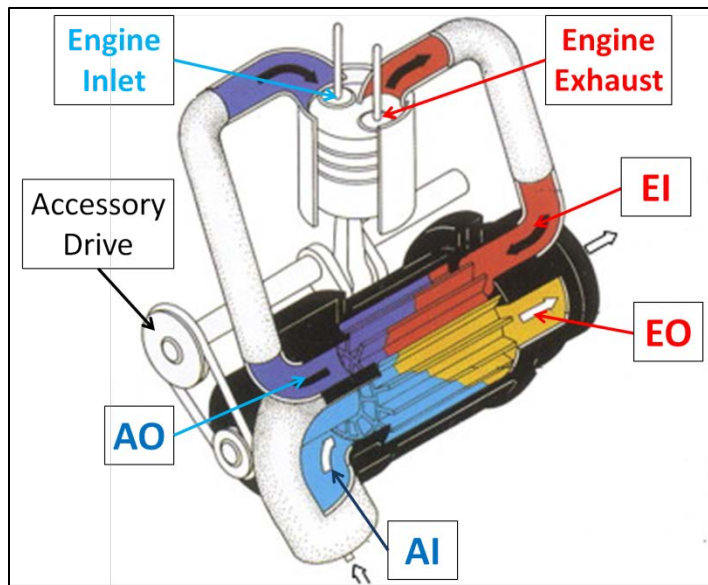
Figure 4: Pressure wave supercharger schematic

Heisler describes the four phases as follows:

1. In the cell compression phase, exhaust gas continuously discharged from the engine's manifold enters the wave rotor through the exhaust inlet port (EI) and flows into a momentarily aligned channel of the revolving rotor. The introduction of the exhaust gas' kinetic energy into the existing fresh air in the channel generates a pressure wave. The pressure wave moves through the air in the channel, at sonic speed, to the other end of the rotor.

2. In the cylinder filling phase, the pressure wave created by the entering exhaust gas in the cell compression phase, simultaneously compresses and accelerates the fresh air trapped in the revolving rotor channel. The channel then aligns with the air exit port (AO), causing the compressed air to be driven out through AO into the engine air intake manifold. The channel is only open to AO for a short time. This allows for the channel to be closed to the AO port prior to the exhaust gases flowing out AO and into the engine intake manifold.

3. In the cell exhaust gas expulsion phase, the rotor rotates such that the exhaust side of the revolving rotor is aligned with the exhaust exit port (EO). This allows the energized exhaust gas to expand and exit into the vehicle's exhaust system.

4. In the cell filling phase, the exhaust gas exiting EO creates a vacuum in the channel. Soon after the channel is opened EO, the other end of the rotor is opened to the air inlet port (AI). The fresh air at atmospheric pressure, rushes into the lower pressure channels. This results in the fresh air flowing straight through the channel exposed to AI and exiting EO and provides a scavenging and cooling effect. With the channel full of fresh air, it will again align with the EI port and the process will begin again.

The rotation time of the rotor is set so that right after the pressure of the two gases has equalized, the pressurized fresh air is opened to an outlet port on the endplate leading to the engine air intake. This port is only open to the rotor cell for the time required for the air to exit and is then closed so the depressurized exhaust gas does not enter the engine with the air. The rotor cell is then opened to an exhaust port on the other endplate

13

to allow the gas to exit. This is a continuous process allowing for a constant supply of pressurized fresh air to the outlet of the endplate provided a continuous supply of high pressure exhaust gas is at the exhaust inlet.

Heisler (15) states that a basic wave rotor can only operate over a narrow speed and load range since the rotor speed must be matched to the wave travel time. As such, the PWS would only be able to operate at 15% above or below the matched speed condition. Since an automobile's engine speed varies greatly and the engine speed dictates the rotor speed, a solution for off design performance had to be developed. The Comprex® solves this problem with the creation of pockets in both endwalls shown in Figure 5. These pockets alter the end flow boundary conditions creating additional pressure waves to regulate the response to changes of engine speed and load (15). Gyarmathy (16) explains that the pocket design was used to prevent the hard reflections that would occur if the shock wave were to contact a solid wall. These hard reflections would cause a great change in the flow speed and cause flow non-uniformities.
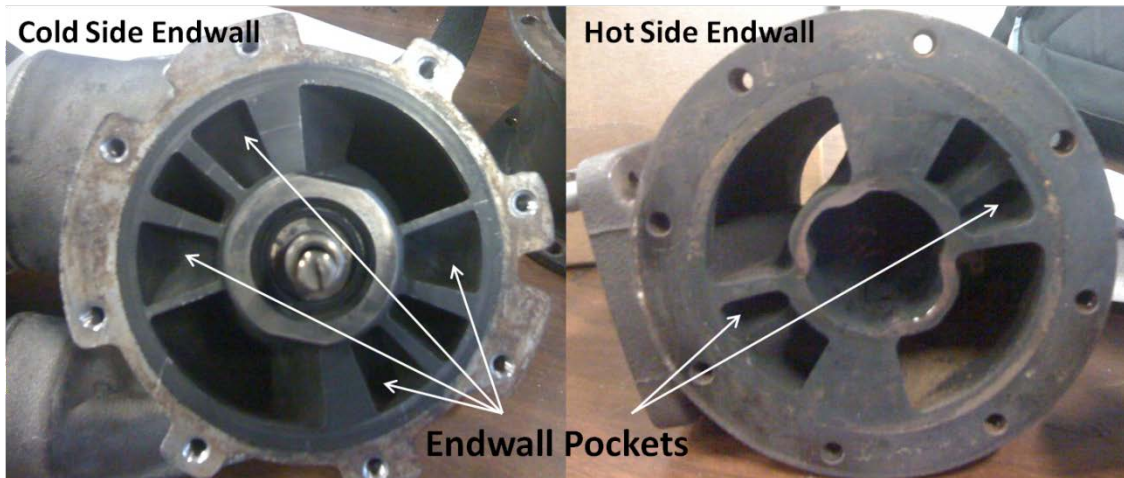
Figure 5: Endwall Pockets

The cold side endwall (containing air in and air out ports) has two pockets, one expansion and one compression pocket, per cycle. The hot side has only one per cycle called the gas pocket. The compression pocket on the cold side endwall mitigates the reflection of the primary shock during low speed operation and cause a pre-compression of the charge air (16). The gas pocket on the hot endwall and the expansion pocket on the cold endwall help to maintain scavenging during all off design operations (16). This is important because insufficient scavenging would lead to engine suffocation from exhaust gas recirculation.

II.5 Pressure Wave Supercharger Advantages

There are many advantages to using a PWS over traditional turbochargers and superchargers. A supercharger requires turbo-machinery to be run off the engine in order to compress the incoming air. While the PWS is run off a belt from the engine, the power provided by the engine is only required to overcome bearing friction. The pressure waves are actually doing the work on the air. The angled air in and exhaust in ports provide the air with a tangential velocity that turns the rotor. This means the PWS will pull far less power from the engine than a supercharger which relies solely on the engine drive to rotate the turbo machinery and compress the air. A typical supercharger can take 50 HP from the engine to operate. As quoted by Heisler (15), the Comprex® needs to pull only 1% of the engine's total power (0.76 HP for the 2.0 liter Mazda engine) for operation.

When compared with a turbocharger, a PWS has much better response time to engine acceleration, (i.e., no turbo lag). Turbo lag is present in turbochargers due to the reliance on the volume of exhaust gases from the engine to turn the turbocharger. At low idle and low engine speeds, the volume of exhaust is small and therefore is not able to provide sufficient mass flow to spin the turbocharger to a speed that would allow aerodynamic compression. This means at low speeds, the turbocharger provides little compression to the air entering the engine inlet. Since the Comprex® relies only on the pressure of the exhaust exiting the vehicle, not the volume, and the exhaust pressure is always greater than atmospheric pressure, the PWS is able to provide compression of the air at all engine speeds.
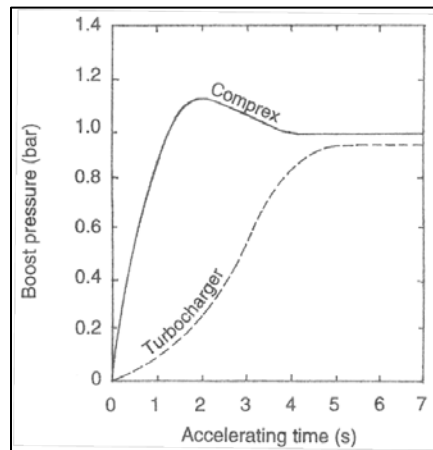
Figure 6: Acceleration response of turbocharger versus Comprex®

As shown in Figure 6, the Comprex® is able to provide ten times the pressure boost of the turbocharger at one second of acceleration. The turbocharger shown in Figure 6 takes four seconds of acceleration time before it reaches its maximum boost capability. The Comprex® achieves maximum boost pressure at 2 second. The

Comprex® also maintains a higher boost pressure throughout the acceleration, even once both have hit their steady state running conditions.

Another potential advantage and a primary focus in the present study is that a PWS may exhibit less efficiency loss than conventional turbochargers with size reduction (11) making it more suitable for scaling to fit smaller engines. In their quest to develop a micro gas turbine capable of producing power in the kilowatt range, Okamoto and Nagashima (17) at the University of Tokyo have produced a wave rotor with a length of 69 mm and a diameter of 47 mm. This is a 78% reduction in the volume of the rotor compared with a Comprex® CX-93. Using the wave rotor characteristic correlation, Iancu et al. (18) at Michigan State University calculated the isentropic compression efficiency of the University of Tokyo wave rotor to be 79%. This estimate of efficiency for the smaller wave rotor, when compared with 83% efficiency quoted by Gyarmathy (16) in a larger scale wave rotor, indicate that this supercharging method may have a scaling advantage over traditional turbo-machinery methods. This possible scaling advantage is the main thrust behind pursuing this method as a means to turbo-normalize a small internal combustion engine.

II.6 Wave Rotor Simulation

The wave rotor computational fluid dynamic code to be used in this research was developed at NASA Glenn Research Center (GRC) by Wilson et al. in the design of their wave rotor used as a turbine topping cycle (19). Since its development, the code has been used in the simulation of a variety of wave rotor applications (20, 21, 22), but has never been used to simulate the Comprex®.

As described by Paxson et al. (23), traditionally, wave rotors were simulated using inviscid compressible gas-dynamic theory or unsteady acoustic theory. These codes also assumed instant opening of the passage ends to the ports similar to a shock tube. The final assumption made by these codes is that the circumferential velocity of the rotor is small compared to the axial velocities. Paxson et al. stated in (24) that these assumptions have led to predictions that do not closely match experimental results. The NASA GRC wave rotor code differs from other wave rotor simulations in that it assumes finite time passage opening, leakage from the passage ends, viscosity, and heat transfer to and from the passage ends (23). The NASA GRC code also accounts for the circumferential velocity of the rotor.

II.7 Other Wave Rotor Research

Wave rotor technology is currently being studied for use in many engine applications. These technologies vary from its traditional use as a supercharger for passenger cars to gas turbine topping cycles to self contained wave rotor engines. Many organizations, including Akbari et al. of Michigan State University (25) and Wilson et al. of the NASA Glenn Research Center (19), have done research into using a wave rotor as a topping cycle in a traditional turbine engine in order to obtain a higher overall efficiency from the turbine (19). For this application, the wave rotor is placed in parallel with the combustion chamber (Figure 7). Air from the compressor is directed into the wave rotor where it is further compressed by a series of shock waves resulting from air from a second stream. The air then leaves the wave rotor, at a higher pressure than it entered, to the combustor. After being heated in the combustor, the gas returns to the

wave rotor as the second stream thus providing the shock to compress the air from the compressor. The exit from the port leading to the combustor is positioned such that the gas from the compressor will be allowed to exit, but the passage closes prior to the gas from the combustor reaching the port. The gas from the combustor is then released through an exit port where it expands. The air then enters the turbine section of the engine (19). Since the air through the wave rotor is first compressed and then expanded, the wave rotor topping cycle performs the functions of both the compressor and turbine in the high spool (19).
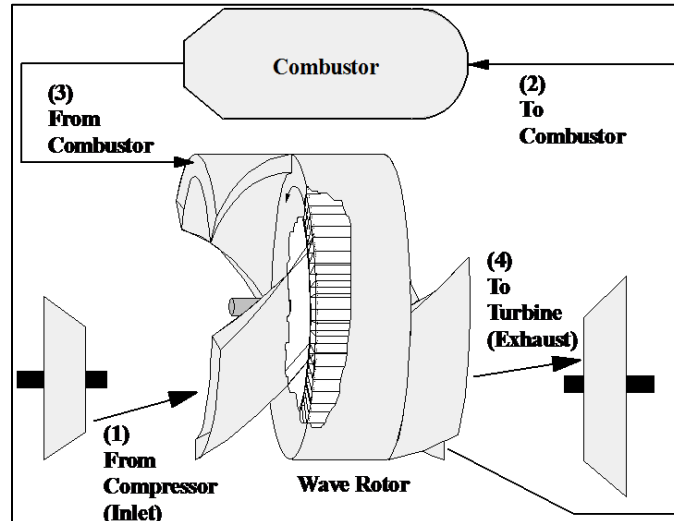
Figure 7: Schematic diagram of a wave rotor turbine topping cycle (19)

The addition of the wave rotor as a turbine topping cycle has produced large increases in specific power and reductions in specific fuel consumption. As seen in Figure 8, at a turbine inlet temperature of 2400° R and a shaft compression ratio of 8, the addition of the wave rotor topping cycle (dashed line; solid line is without turbine topping cycle) increases specific power by 19.2% (19). Figure 9 shows that at the same conditions, the specific fuel consumption is reduced by 16.2% (19).

19
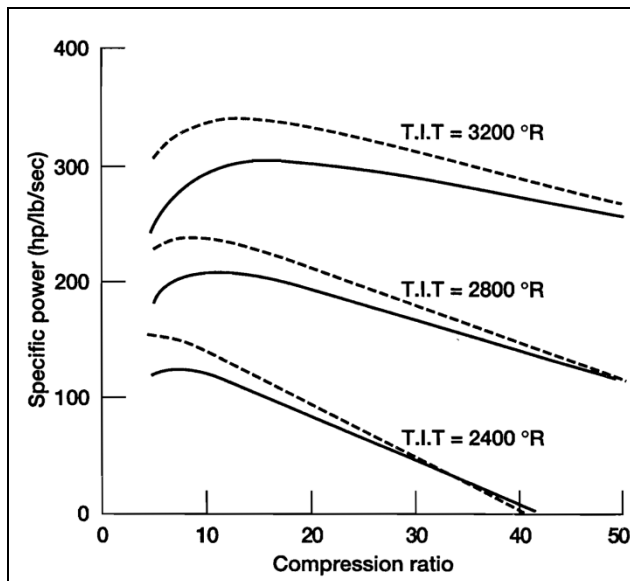
Figure 8: Power comparison with and without turbine topping cycle (19)
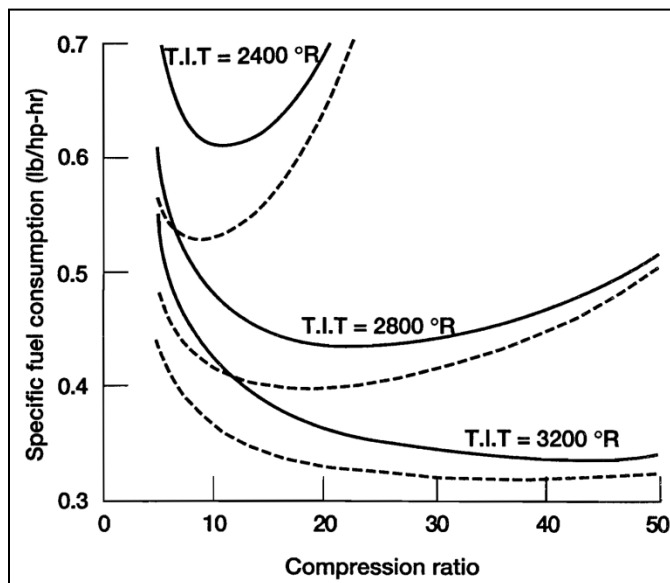
Figure 9: Specific fuel consumption comparison with and without turbine topping cycle (19)
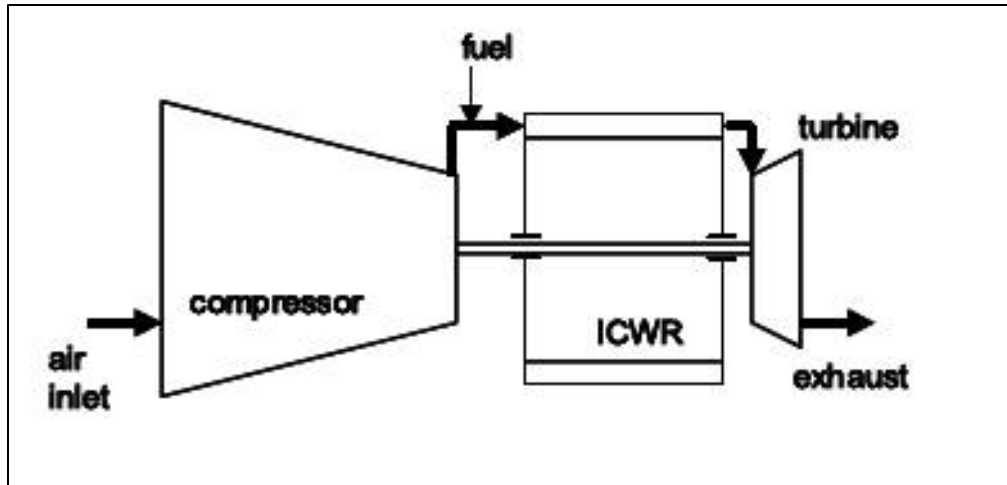
Figure 10: Schematic diagram of an internal combustion wave rotor (26)

Indiana University Purdue University of Indianapolis (IUPUI) is currently

developing an internal combustion wave rotor (ICWR) shown in Figure 10. Nalim et al

describes that in the ICWR, combustion would occur sequentially within the wave rotor

channels (26). It acts as a revolving series of pulse detonation tubes. In stationary-

channel pulsed engines, the shutter valves used introduce a lot of unsteadiness to the fluid

flow. The wave rotor acts as a high speed valve for the engine. This provides nearly

steady inflow and outflow of the passages. The rotational nature of the ICRW allows for

a single steady ignition device for multiple tubes. To achieve these advantages, each

channel is charged and discharged as it rotates past inlet and outlet port. The channel is

filled with a premixed air-fuel combination and then, with a spark igniter or hot gas

injection duct, deflagration or detonation waves are initiated. This wave rotor device

would eliminate the need for an external combustion chamber (Figure 8) and its

associated ducting, but will retain the benefits of the wave rotor turbine topping cycle.

Besides the reduction in the required hardware, due to the nature of wave rotors, the

ICWR could allow for more than one cycle per rotation improving mechanical load

21

balancing (26). As proven through research and the operation of prototype engines, the ICRW has potential to achieve high performance gains in a compact system.

Akbari et al. at Michigan State University (25) have been researching the use of wave rotors as condensers in refrigeration applications using water (R718) as the refrigerant. R718 units have been commercialized in Europe. Though the refrigerant cost is low environmentally friendly, the systems are very large in size and have high manufacturing costs. The large size is due to the use of two centrifugal compressors and voluminous internal direct heat exchangers. The high cost is due to expensive specially built compressors with independent variable speed drives. The researchers contest that the use of a condensing wave rotor in water refrigeration cycles can eliminate these challenges that have hindered the wide application of R718 in cooling systems.

Figure 11 shows the condensing wave rotor system would consist of a three port condensing wave rotor replacing the condenser and one of the compressor stages used in the current system. In the wave rotor enhanced cycle, condensation occurs inside the wave rotor channels by compressing the low pressure vapor (State 2 in Figure 9) using the high pressure water (State 6 in Figure 9). The liquid water at an intermediate pressure is discharged from the rotor channels. The compressor stage eliminated from the original system is replaced by the pressure gain generated by shock waves inside the channels. The condensing wave rotor employs pressurized water to pressurize, de-superheat, and condense the superheated vapor coming from the compressor - all in one dynamic process.
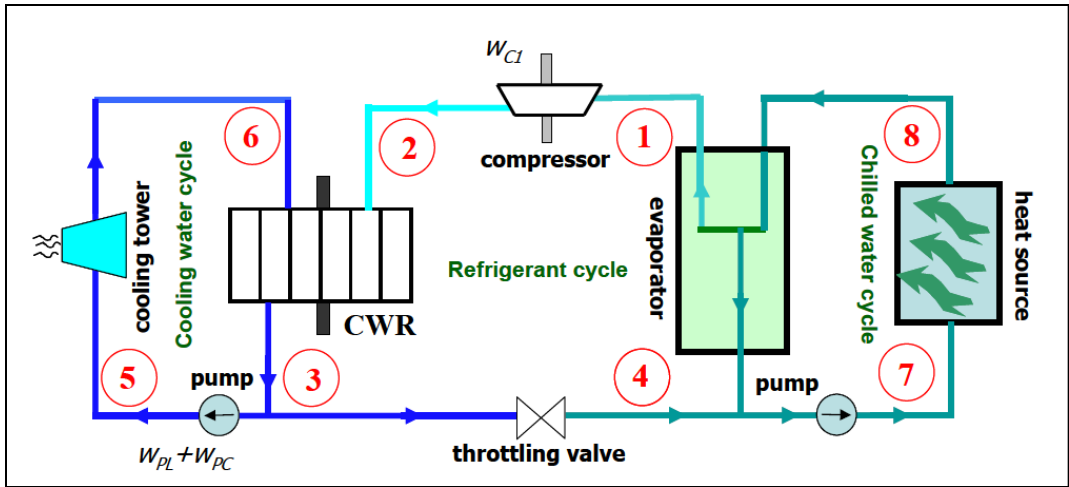
Figure 11: Schematic of R718 cooling unit enhanced by a condensing wave rotor (25)

The condensing wave rotor port configuration (Figure 12) is similar to those of the pressure wave supercharger, but the cycle differs by the phase changes inside the channels (25).
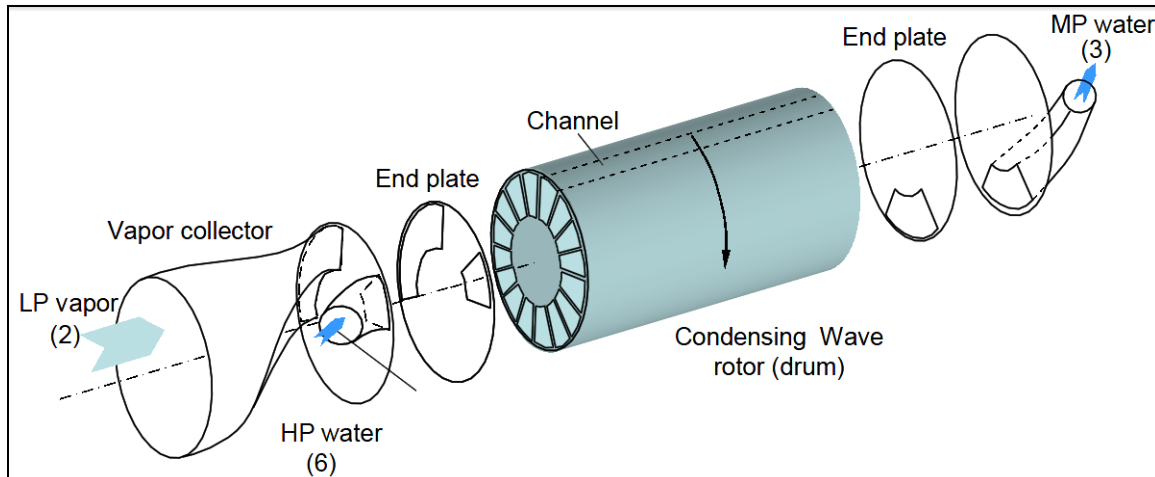
Figure 12: Schematic of three point condensing wave rotor (18)

Kharazi et al. (26) explains that the cycle for the condensing wave rotor consists of low pressure, superheated water vapor entering through Port 2 in Figure 11. The rotor then rotates to align the channels with Port 6 in Figure 11 and the cells are filled with

high pressure, low temperature water. The water absorbs much of the heat in the vapor

allowing it to condense to saturated water vapor. The water, which in now condensed

due to the latent heat of the vapor, exits via Port 3 in Figure 11. Simulations show that

the wave rotor enhanced cycle improves the coefficient of performance by 22% over the

baseline system.

III. Experimental Setup

The objectives of this research are four fold. Phase One was to experimentally characterize the performance of the Comprex® pressure wave supercharger. Phase Two was the validation of wave rotor simulation code developed by Dr. Dan Paxson of the NASA John H. Glenn Research Center (NASA GRC) for the Comprex® wave rotor. This objective consisted of running a modified version of the NASA code at actual experimental condition and comparing the code predicted parameters with the experimental data collected on the Comprex® in Phase One. Phase Three was to design a pressure wave supercharger scaled to be used on a 95cc Brison engine. The final phase was to use the validated NASA GRC code to simulate the performance of the scaled supercharger. This chapter will discuss the tools needed to achieve these objectives. These tools include the experimental setup, the NASA GRC CFD code, and the equations for pressure wave supercharger design.

III.1 Comprex® Characterization Experimental Setup

For the validation of NASA GRC's code, a Comprex® CX-93 (Figure 13) used on a Mazda 626 Capella was obtained from Dr. Razi Nalim of the University of Indiana - Purdue University of Indianapolis. The simulation code validation required that a set of data points be experimentally obtained through laboratory simulation of the Comprex's® running environment. Running the same conditions in the simulation code enabled the correlation between the experimentally obtained and computational results. In order to match the data from the CFD code, the pressures, temperatures, and mass flow rates at

each port had to be known. To achieve this, The Mazda 626, 2.0L engine conditions were replicated in a laboratory environment.

Figure 13: Comprex® CX-93 on and off the Mazda 2.0L diesel engine

The simulation of the engine was accomplished though the replication of the two primary engine interfaces with the pressure wave supercharger: the engine exhaust and the accessory drive. Figure 14 is a diagram of the experimental setup used to gather the needed information on the Comprex®. The exhaust was modeled with compressed air that has passed through heaters. The accessory drive was replicated with an electric motor driving a belt and pulley system to rotate the Comprex®.
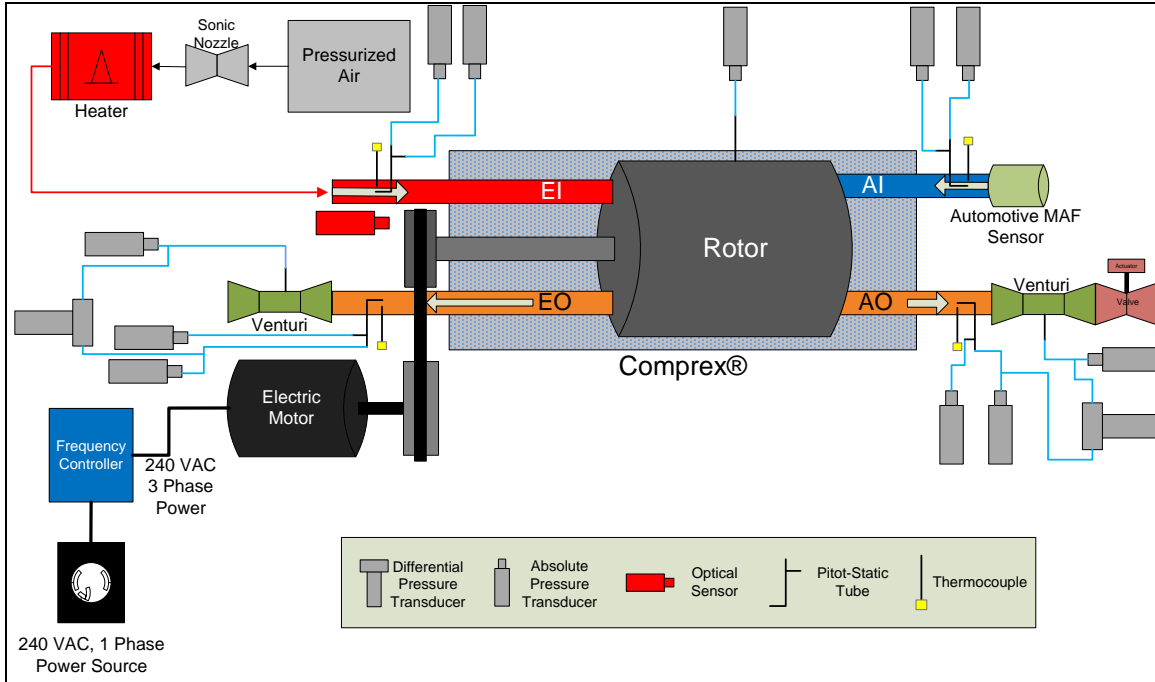
Figure 14: Experimental setup schematic

In order to properly simulate the exhaust conditions, the mass flow into the Comprex® at

the exhaust in port (EI) had to be consistent with what the diesel engine would produce at

each operating point tested. Equation 1 shows how to calculate the volumetric flow rate

an engine requires. It was used to calculate the required volumetric flow rate at each

engine speed where D is the engine displacement in cubic feet, N is the engine speed in

revolutions per minute and VE is the volumetric efficiency. For simplification, the

volumetric efficiency was assumed to be unity.

$$\dot{V} = \frac{D*N*VE}{60} \qquad (1)$$

The volumetric flow rate calculated using Equation 1 is for a naturally aspirated

engine. Since the Comprex® supercharges the air, increasing the pressure to

approximately twice that of atmospheric pressure, the volumetric flow rate calculated

must be doubled to send the required volume of air to the engine. Equation 1 is intended

to calculate the air flow into the engine, but since the mass entering the engine must equal

the mass leaving (neglecting fuel), it can also be used as the volumetric flow out of the

exhaust system.

Using the density at the ambient temperature and the volumetric flow rate, the

mass flow can be determined using Equation 2.

$$\dot{m} = \dot{V} * \rho \qquad\qquad (2)$$

Since the mass entering the engine must be the same as the mass leaving the calculated

mass flow was used as the mass flow put into the exhaust in (EI) port of the Comprex®.

Table 1 shows the required volumetric and mass flow rates at a range of engine speeds.

Table 1: Flow rates for given engine speed in Mazda 626 2.0L diesel

Engine Speed (RPM)	Volumetric Flow Rate (ft^3/min)	Mass Flow Rate (lb/min)
1000	70.63	5.30
1500	105.95	7.95
2000	141.26	10.59
2500	176.58	13.11
3000	211.89	15.89
3500	247.21	18.54
4000	282.52	21.19
4500	317.84	23.84

To provide the proper mass flow to the EI port, a sonic nozzle with a diameter of

0.494" was located in the air supply line. The mass flow through the system is managed

with the sonic nozzle. Mass flow was controlled by adjusting the pressure upstream of the

nozzle. The mass flow through the nozzle is determined by using the total pressure and

temperature upstream and the nozzle throat area in the mass flow equation for an ideal

compressible gas (Equation 3).

$$\dot{m} = \frac{A*p_t}{\sqrt{T_t}} * \sqrt{\frac{\gamma}{R}} * M(1 + \frac{\gamma-1}{2} * M^2)^{-\frac{\gamma+1}{2(\gamma-1)}} \qquad (3)$$

Since the flow is sonic (M=1) at the throat, Equation 3 can be reduced to Equation 4.

$$\dot{m} = \frac{A*p_t}{\sqrt{T_t}} * \sqrt{\frac{\gamma}{R}} * (\frac{\gamma+1}{2})^{-\frac{\gamma+1}{2(\gamma-1)}} \qquad (4)$$

Since the throat area (A) and total temperature (T_t) are known and the specific heat ratio

(γ) and gas constant (R) are constants, the mass flow can be controlled by simply

controlling the upstream total pressure.

The temperature of the air entering the engine must also be controlled. The

temperature is increased using two Chromalox GCHISR 20 kilowatt heaters located

downstream of the sonic nozzle. Rearranging the simplified steady flow thermal energy

equation (27) (Equation 5), the maximum temperature change for the available energy

can be calculated.

$$\Delta T = \frac{q}{\dot{m}c_p} \qquad (5)$$

Ideally the air entering through EI would be near 1520 R, but at the required flow rates,

this temperature was not achievable. Since the goal of this phase of the research is to

obtain data to validate the NASA GRC wave rotor code, the simulation was run at the

operating conditions at which the data was taken and compared with the experimental

data for those conditions. Due to the heater restrictions, the maximum temperatures

achieved varied with the mass flow flowing into the system. Table 2 shows the

maximum temperatures achieved for each mass flow tested.

Table 2: Maximum temperature at flow rates

Mass Flow (lb/min)	Maximum Temperature (R)
13.1	883
15.9	870

The accessory drive was replicated using a Dayton 4THV6 2 horsepower 230 volt

3 phase alternating current electric motor (Figure 15) with an 8.1" diameter pulley. The

pulley was connected to the Comprex® via a 3VX belt to turn the rotor. The motor has a

manufacture stated maximum RPM of 3480. Through the use of a Fuji FRN002C1S-7U

(Figure 16) adjustable frequency drive, the motor's rotational speed was adjustable

throughout the motor's operating range.

Figure 15: Dayton 2 HP electric motor

Figure 16: Fuji adjustable frequency control

Because the electric motor's RPM range does not match that of the Mazda engine, the

pulley ratio was increased to 5:1 vice the 4.25:1 used on the original diesel engine. With

the increased pulley ratio, the electric motor was able to spin the Comprex® rotor to

15,000 RPM. This correlated to the Mazda engine operating up to approximately 3,500

RPM, which was the near the top of the normal operating range of the automobile.

III.1.2 Pressure, Temperature, and Mass Flow Measurements

With the engine exhaust simulated, the focus turned to gathering the data required

to compare the experimental results with the simulation predictions. As previously

mentioned, the pressure, temperature, and mass flow at each port was required for this

comparison. The pressure and temperature measurements were used in the calculation of

the mass flows in the comparison of the simulated to the experimental results. While the

mass flows were also used in the comparison the two sets of results, they were also the

primary indication that the Comprex® was operating properly. When in actual engine

operation, the mass flow that entered the engine (the air leaving the Comprex® via AO)

must match the mass flow of the exhaust exiting the engine (the gas that enters the

Comprex® via EI). This means that the mass flows at AI and EO should be equal when simulating engine condition. This also indicated that the mass flows at AI and EO must also be equal to ensure mass was conserved. As previously discussed, the Comprex® uses scavenge air to ensure the channels were completely evacuated of exhaust prior to filling with air and that there was a buffer of extra air between the exhaust and air interaction. Because of this scavenge air, the mass flows at AI and EO should be higher than the mass flows AO and EI.

To measure the pressure, a 1/8" Dwyer 166-6-CF pitot-static probe was placed in the tube leading to each port just downstream of the entrance to the port using a compression fitting screwed into a flush mounted bung. As shown in Figure 17, the total pressure probe was placed in the center of the tube. The total and static ports of the pitot-static tube were connected to an Omegadyne PX-219, 60 psi absolute pressure transducer with 1/8" inner diameter tygon tubing. The tubing was secured to the total and static pressure taps with hose clamps and to the pressure transducers with Swagelok fittings. The pressure transducers were remotely mounted to avoid the high temperatures of the Comprex® and the air inside when operating. 1/16" Watlow K-type thermocouples were placed at the end of and ½" above the total pressure at each port using Swagelok fittings screwed into a bung welded to the tube.
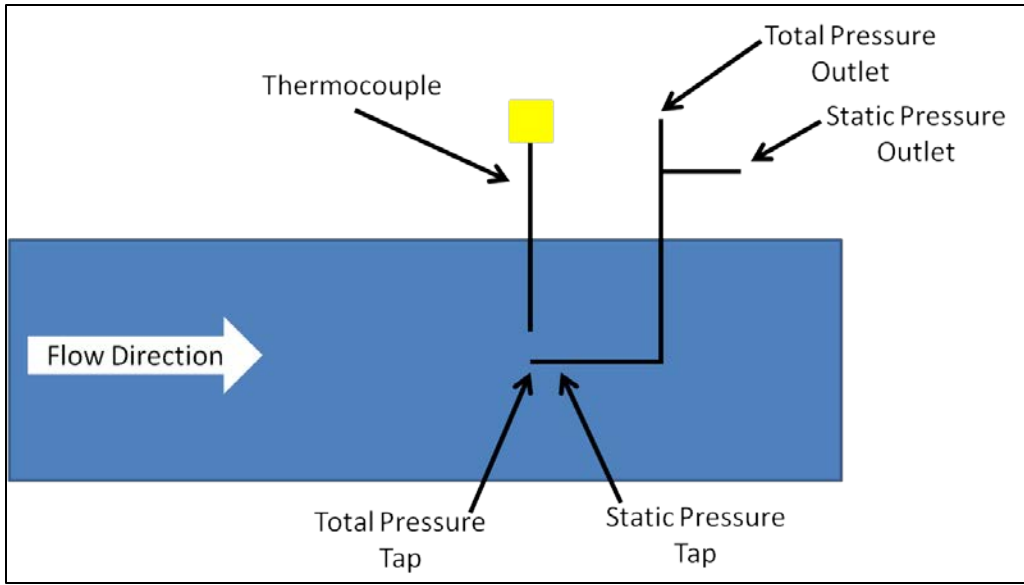
Figure 17: Pitot-static probe and thermocouple layout

The air to be compressed comes into the Comprex® from the atmosphere via the air in port (AI). In the actual engine, this would be the air entering through the air filter and into the engine. To measure the flow rate of the air entering AI, a Pro-M Racing 75 mm automotive mass air flow (MAF) sensor, shown in Figure 18 was used. To straighten the air flow into the system, the air filter was removed and an aluminum honeycomb with 3/16" cells was fixed up stream of the MAF (Figure 19). The flow straightener ensured that any air disturbed by other parts of the test rig en route to AI would be laminar before reaching the MAF.

Figure 18: Pro-M Racing 75BD mass air flow sensor
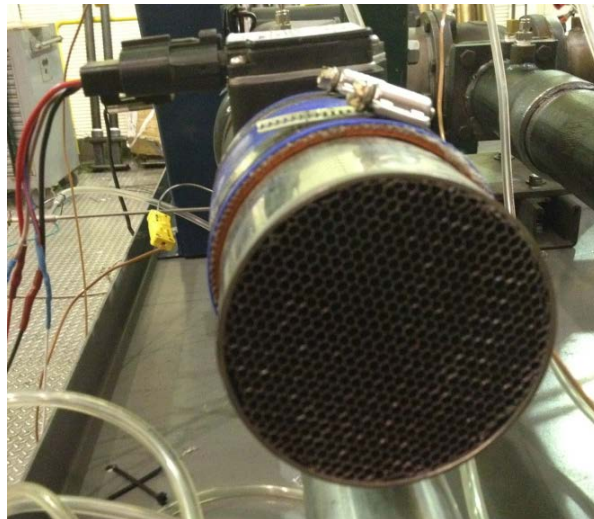
Figure 19: Honeycomb air flow straightener

The flow out of the air out port (AO) required a metering device that would allow for the mass flow exiting the port to be controlled. To achieve this, a Dwyer Instruments GV-2, 2" globe valve was paired with a Dwyer Instruments EVA2 electronic valve actuator (Figure 20). The addition of the actuator enabled remote control of the valve via a 0-10 Volt DC control signal and a 24 Volt AC power supply. This control was essential to ensuring the mass flow leaving the AO port and the mass flow of the gas entering the

EI port are equal, as discussed above. Limiting the exit area at AO forces the excess gas

to exit via the EO port. This allows the mass flow out of each of the exit ports to be

controlled thus enabling the mass flows at AO and EI and EO and AI to be properly

matched.
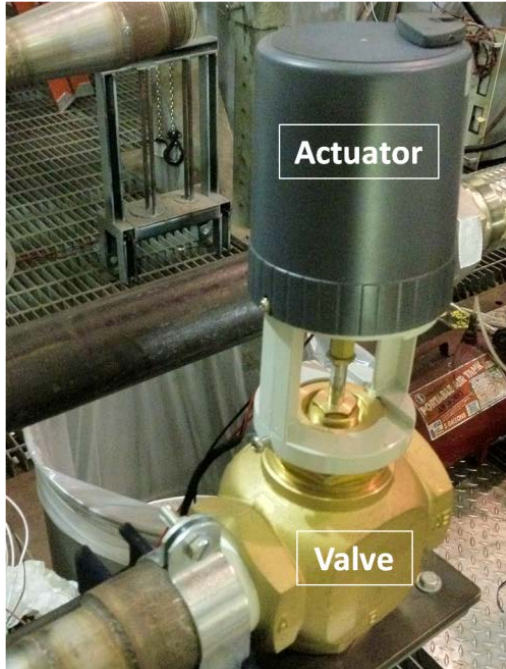
Figure 20: AO valve and electric actuator

In order to monitor the mass flow out AO, a venturi device was built by the author

(Figure 21). The venturi was built using two stainless steel 2" to 1" reducing fittings on

each end of a short length of 1" tubing as the throat. Four pressure taps made of 1/8"

stainless steel tubing were mounted equally spaced around the circumference of the throat

of the venturi and flush with the inner wall of the tube. The pressure taps were connected

to a square manifold with equal lengths of 1/8" ID tygon tubing. An Omegadyne PX-409

15 psi differential pressure transducer was connected to the outlet of the manifold and the

total pressure tap located upstream. This pressure difference was used to calculate the

mass flow through the venturi.
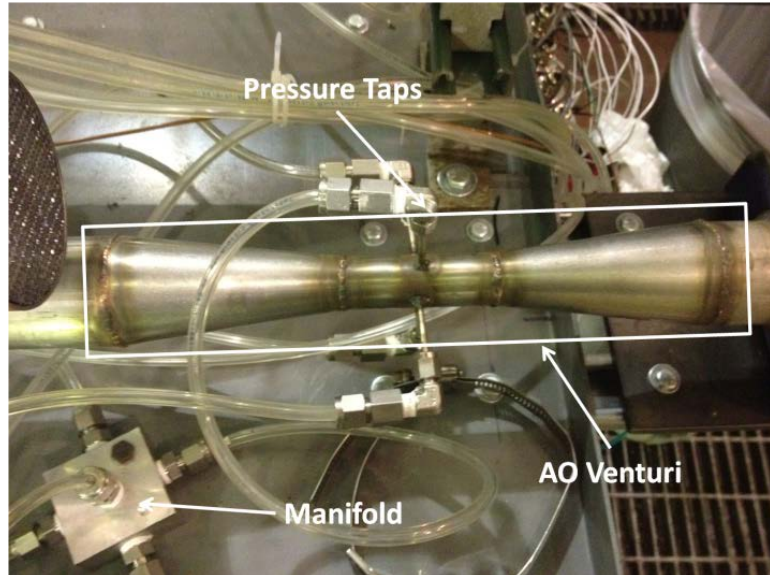
Figure 21: Venturi at AO

The final port to be instrumented was the exhaust out (EO) port. This port would

provide the exhaust gases leaving via the exhaust system in the actual engine. The mass

flow leaving EO was measured using a venturi similar to the one used on AO, but larger.

The tube leading out of the EO port was 3" in diameter, therefore the venturi was

constructed using two 3" to 2" reducing fittings and a short length of 2" tubing for the

throat. Again, static pressure taps were mounted every 90° around the circumference of

the throat and were flush with the interior wall of the 2" tube. The static pressure taps

were again run to a square manifold with equal lengths of 1/8" tygon tubing. An

Omegadyne PX-409 5 psi differential pressure transducer was connected to the manifold

outlet and the total pressure tap of the upstream pitot-static tube.

A Transcat ROS-W remote optical sensor was used to gather the Comprex® rotor speed. The sensor detects the passing of a piece of reflective tape affixed to the rotating object. Each time the tape was sensed, the voltage dropped to nearly 0 Volts DC. For use in this experiment, the reflective tape was placed on the pulley driving the Comprex® rotor. The sensor was mounted to the belt guard (Figure 22) so that the Comprex® pulley and the tape were visible.
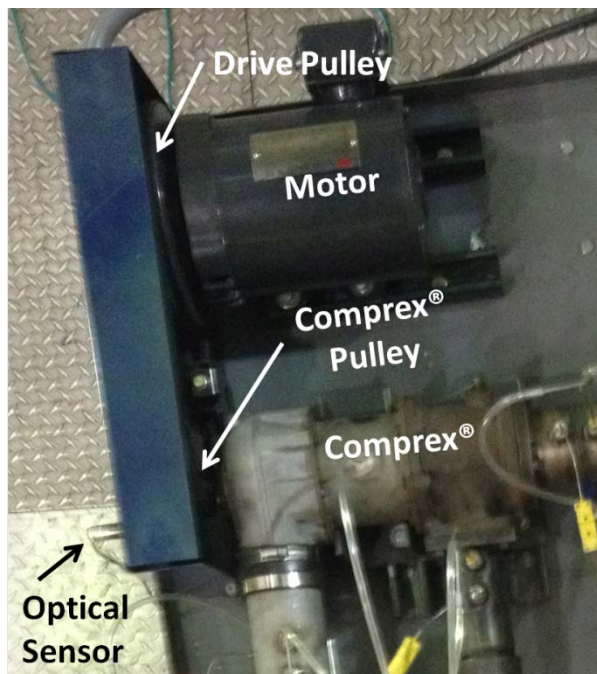
Figure 22: Optical sensor placement

III.1.3 Data Acquisition

A National Instruments cDAQ-9188 eight slot Ethernet compact data acquisition chassis was used to gather the incoming data from the sensors (Figure 23). This chassis allows for control and monitoring of the installed modules via an Ethernet cable. For this experimental setup, the Ethernet cable was run from the chassis to a laptop computer

located in the control room. The Ethernet connection allowed for full control and

monitoring ability of every sensor while safely located in the control room.

Figure 23: Data acquisition chassis

The chassis was loaded with four data acquisition modules. The NI 9402 is a four

channel bidirectional digital input module. It was used to get the signal from the

Comprex® pulley optical sensor. An NI 9205 16 bit, ±10 Volts DC, analog input module

was used to gather the pressure transducer data. For the thermocouple data, an NI 9213

module was used. This is a thermocouple specific module with built in cold junction

compensation. The final module used was the NI 9264. This module provides a -10 to

10 Volts DC output signal and was used as the control signal for the AO valve actuator

and to provide remote control for the adjustable frequency controller for the motor.

Figure 24 shows all the modules installed in the chassis and wired for operation.
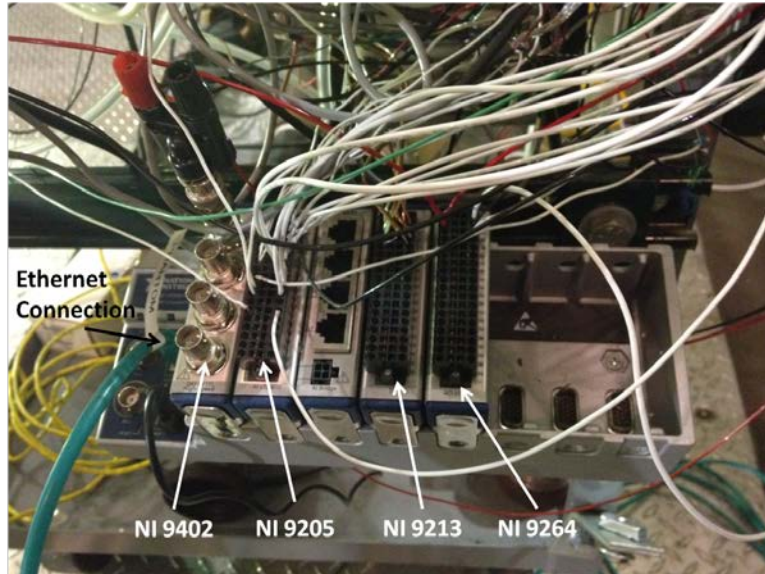
Figure 24: Data acquisition chassis with modules

All the sensors used required a 12 Volt DC power signal. Power was provided with a TDK Lambda ZUP36-12/U power supply. The power from the Lambda was run to a set of terminal blocks (Figure 25) to distribute power to each sensor. The negative terminal of the power supply and the common for each sensor were also run to a terminal block to ensure each sensor shared a common reference signal. The earth ground of the power supply and the grounding for each sensor were run to a third terminal block. Finally the common and ground terminal blocks were wired together to make the reference signal and earth ground coincide.
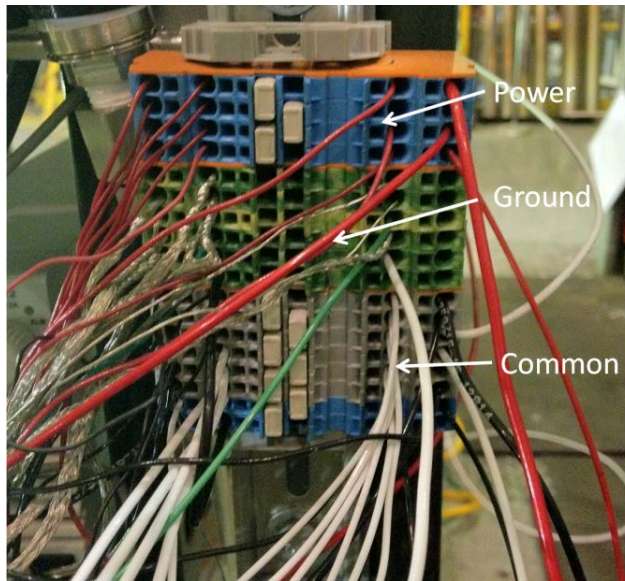
Figure 25: Terminal block

The data acquisition system was controlled with a National Instruments

LabVIEW based acquisition program (Figure 26).

Figure 26: LabVIEW screen shot

The LabVIEW code allowed for the temperatures, total and static pressures and

Comprex® speed to be monitored and recorded. The program also gave full control of

the motor speed via the remote control of the Fuji frequency controller and the AO valve

opening by varying the signal output to the valve actuator from 0-10 Volts DC.

III.1.4 Calibration

In order to achieve accurate data from the data acquisition system, each of the

sensors used needed to be calibrated and the calibration loaded into the LabVIEW

program. Each of the pressure transducers came from the manufacturer with a calibration

sheet. The slope of the calibration line and the zero offset from each pressure transducer

was calculated and that value was entered into the LabVIEW code's calibration section

shown in Figure 27. This allowed the program to account for the calibration and output

the actual pressure at each port.
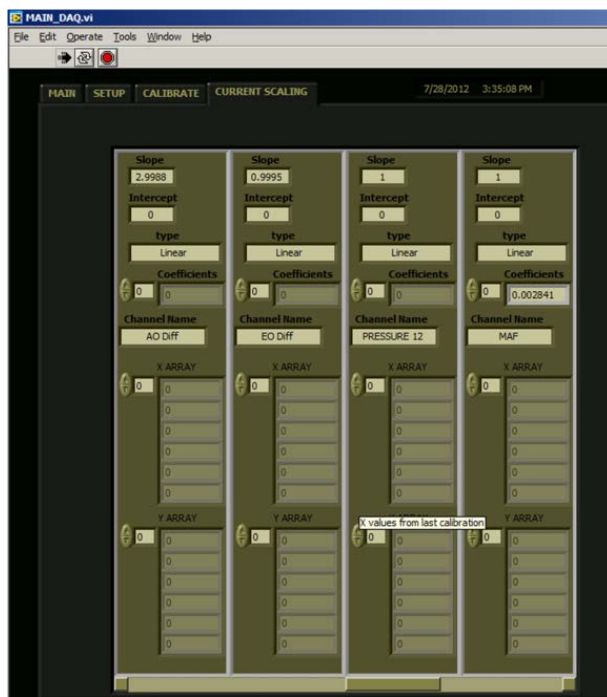
Figure 27: LabVIEW scaling tab

41

The mass airflow sensor on AI and the venturis on AO and EO also had to be calibrated. Since these devices were intended to measure mass flow through the system, a known mass flow had to be provided to each and their outputs recorded at each flow rate. For the MAF sensor calibration, the sensor was plumbed to the outlet of the compressed air system used for EI. The mass flow from the system was changed across the expected range of mass flows for the engine. The voltage output by the MAF was recorded for each mass flow. The results were plotted and a 4th order polynomial curve fit was established (Figure 28).

Mass Air Flow Sensor Calibration

$y = 0.015974x^4 - 0.019825x^3 + 1.150637x^2 - 0.046693x + 0.010150$
$R^2 = 0.997109$

Mass Flow (lb/min) vs MAF Signal (Volts)
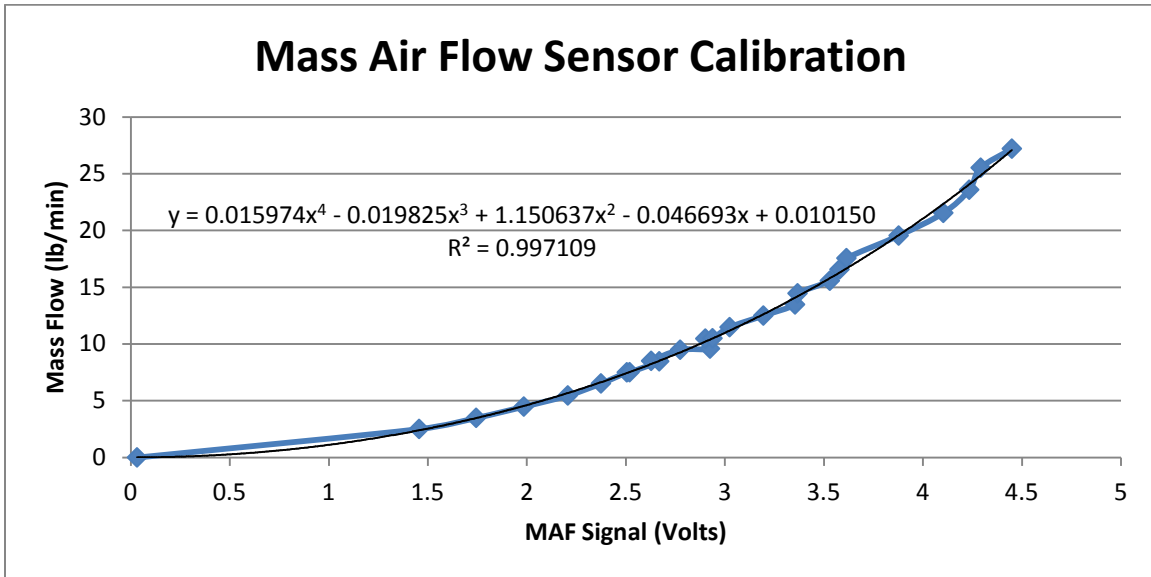
Figure 28: AI mass air flow sensor calibration curve

The calibration process was similar for the venturis at AO and EO, except the pressure differential between the total pressure upstream and the static pressure at the throat were measured and recorded. The mass flow values were plotted versus the difference in pressure between the total upstream pressure and static pressure at the throat of the venturi. For the EO calibration, a 2nd order polynomial curve fit was created. The

calibration curve for the EO venturi is shown in Figure 29. Due to the smaller size of the

throat of the AO, the flow becomes sonic at higher mass flow rates. This required two

separate curve fits to be made to the data set. The first is a second order curve fit at the

low mass flows and a linear curve fit once the flow becomes sonic. The results of these

fits can be seen in Figure 30.
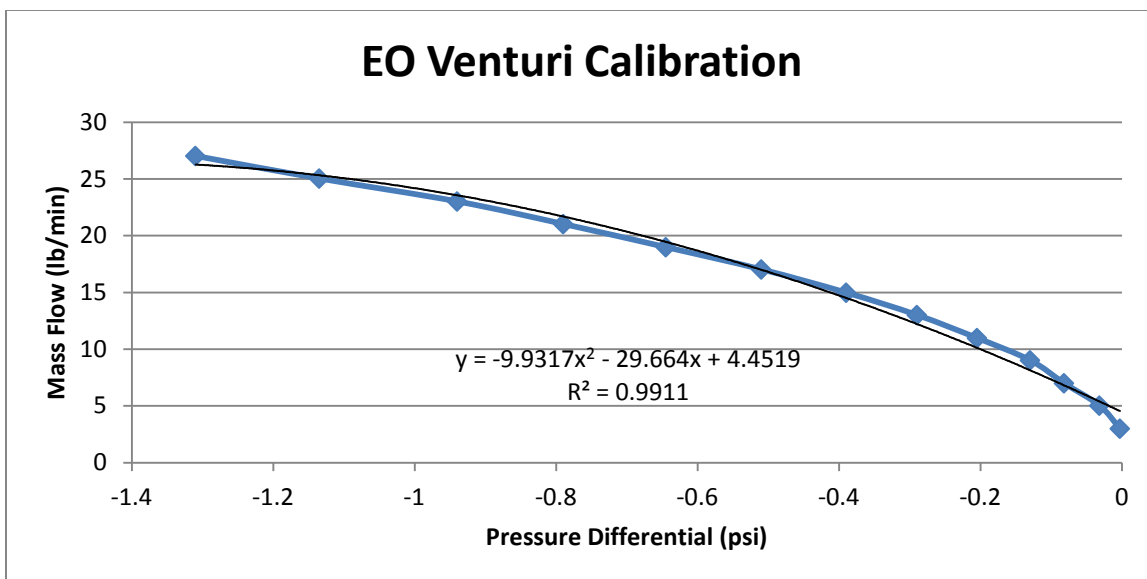
Figure 29: EO venturi calibration curve
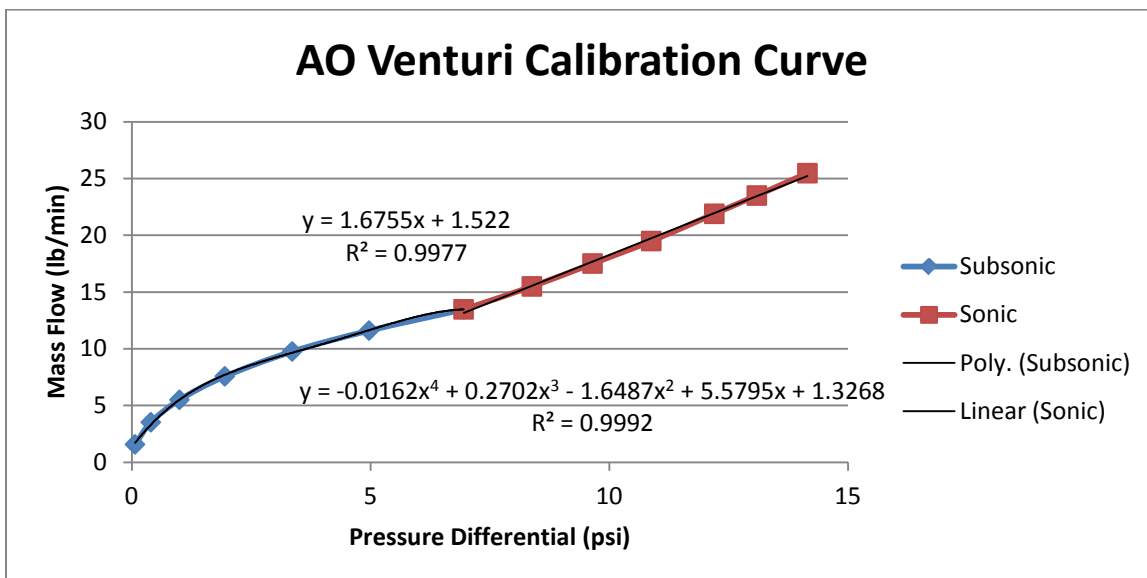
Figure 30: EO venturi calibration curve

43

The coefficients determined from the curve fit of the mass air flow sensor on AI were entered into the LabVIEW calibration page (Figure 27). This allowed the program to output the actual mass flow at any instant in time.

Due to the venturi calibrations being conducted at room temperature, the mass flow calibration curves would not be accurate at the operational temperatures of the Comprex®. Because of this, the calibration curves were used to calculate effective area of the venturi throat using Equation 6 from Holman (28). The mass flow ($\dot{m}$) is known from the sonic nozzle system and the total (P_t) and static (P_s) pressures are known from the pressure transducers. The specific heat ratio (γ) and the gravitational constant (g_c) are known constants.

$$A = \left[\frac{\dot{m}^2}{2g_c\left(\frac{\gamma}{\gamma-1}\right)\left(\frac{P_s}{RT_1}\right)\left[\left(\frac{P_t}{P_s}\right)^{2/\gamma} - \left(\frac{P_t}{P_s}\right)^{(\gamma+1)/\gamma}\right]} \right]^{1/2} \qquad (6)$$

The effective area of the throat of the EO venturi was found to be 2.22 in^2 and the effective area of AO was found to be 0.54 in^2. The discharge coefficient (C_d) can be calculated using Equation 7 where A_{eff} is the effective area and A_{nom} is the nominal area calculated from the manufacturer published nominal diameter. The nominal areas are 2.74 in^2 and 0.59 in^2 for EO and AO respectively.

$$C_d = \frac{A_{eff}}{A_{nom}} \qquad (7)$$

44

The discharge coefficients calculated for EO and AO were 0.81 and 0.91 respectively. These are lower than the 0.98 generally accepted for venturis, but the 0.98 value is for manufactured venturis that are optimized for flow measurement. The venturis used here were handmade using welded tubing which would not provide the optimized conditions for flow measurement.

Since the effective area does not change with temperature, the areas calculated from the calibration curves can be used with Equation 7 (28) to calculate the mass flow through each venturi during the experiments.

$$\dot{m}^2 = 2g_c A_{eff}^2 \left(\frac{\gamma}{\gamma-1}\right) \left(\frac{P_s}{RT_1}\right) \left[\left(\frac{P_t}{P_s}\right)^{2/\gamma} - \left(\frac{P_t}{P_s}\right)^{(\gamma+1)/\gamma}\right] \tag{7}$$

This equation compensates for the actual temperature and pressures of the flow in the venturi, T_1, with P_s being the pressure at the throat and P_t the total pressure upstream of the venturi.

III.2 Simulation Experimental Setup

The simulation of the wave rotor for both the validation of the CFD code and the performance evaluation of the scaled wave rotor supercharger were done using the NASA Glenn Research Center quasi one-dimensional wave rotor computational fluid dynamics code discussed briefly in Chapter II. The GRC wave rotor code is quasi one-dimensional and time accurate. It numerically integrates the mass, momentum, and energy equations for a calorically perfect gas. The code follows a single passage of the wave rotor, as it rotates past the various ports governing the cycle. A second order, Lax-Wendroff

integration scheme is utilized which incorporates Roe's approximate Riemann solver and a flux limiter in order to ensure total variation diminishing behavior, while preserving sharp resolution of shock waves and contact discontinuities. The code includes terms to account for leakage between the passages and the endwalls, wall friction, and wall to gas heat transfer. These terms are derived from previous wave rotor experiments (19, 20). They contain correlations which link their relative strength to physical aspects of the experimental rig (e.g. rotor-to-endwall clearances, passage hydraulic diameter, Prandtl number), and local fluid variables such as velocity and density (30). Source terms are applied globally to those modeling wall friction and heat transfer effects. They are applied discretely in the first and last interior numerical cell for leakage effects.

The NASA GRC Wave Rotor code contains a robust, characteristics-based boundary condition algorithm that permits inflow or outflow at any port, depending on the status of the passage flow and the specified port pressures. This allows simulation of both on and off-design operation. Inflow losses due to incidence, and gradual opening and closing (i.e. throttling of the passage as it rotates into or out of a port region) are also accounted for. The code operates in the passage relative frame, while boundary conditions are specified in the absolute frame. The boundary conditions routines account for this reference frame change as well. When the passage is adjacent to a solid wall, a separate boundary routine is applied which ensures that the flux quantities at the passage end face are zero. The temporal specification of boundary conditions (i.e. which to apply, and when) is determined by the user specified location of the ports, and the rotor speed (23).

Since the code contains a heat transfer model, the rotor wall temperature must be supplied at each numerical cell. Initially, this is chosen as the inlet temperature. The code then computes through one wave cycle (rotor revolution) integrating the total heat flux into or out of the wall at each cell. The heat flux is assumed to occur between the rotor wall and the working fluid and, to a much lesser extent, between the rotor wall and the internal leakage cavity fluid. The rotor housing is assumed adiabatic. At the end of the cycle, the wall temperatures are updated, lumped parameter style, using an arbitrary thermal mass, a first order Euler scheme, and the integrated heat flux. This process is repeated until the wall temperatures stop changing.

Though used to simulate wave rotors in the past (20, 21, 22), this code has not been used to simulate a wave rotor with the scale and geometry of the Comprex®. To be able to use GRC code for this research, three modifications were made to the code by its author, Dr. Dan Paxson.

The first is a simple cavity representing the casing volume not occupied by the rotor. Internal leakage flow travels to and from this volume (via the code source terms) as the passage rotates. The amount and direction of leakage depends on the state of the cavity, and the state of the passage cells where leakage is assumed to occur. The gas state in the cavity is updated each revolution, or cycle, of the rotor. The updating is done via simple Euler integration with a time step equal to the period of one cycle. The integration is not time-accurate, but does not need to be since it is merely used to achieve a steady state result. When the net flow to the cavity over the course of a cycle is zero, convergence has been reached, and the cavity gas state no longer changes.

47

The second additional component, similar to the first was a cavity representing each endwall 'pockets' discussed in Chapter II to which the rotor passages are exposed. Their purpose is to allow off design operation of the device by essentially acting as dampers for spuriously generated gas dynamic waves. In the code, this sculpted endwall section was modeled as a leakage term, with an oversized leakage gap (approximately 50 times the endwall clearance gap). The cavity to and from which this leakage flow travels was treated the same as, but separate from, the casing cavity.

The third additional component was a simple valve model which was placed on the exhaust outlet port. It was used to represent the venturi flow measuring restriction within the experiment. The component consists of an orifice-type flow equation, and dynamic lumped volume mass and energy equations. During each cycle the mass and enthalpy fluxes from the rotor into the volume were computed based on the back pressure imposed on the rotor by the volume. Also computed are the mass and enthalpy fluxes out of the volume and across the valve. The difference between volume inflow and outflow were then used to update the back pressure each cycle. When there was no longer a difference, the back pressure no longer changes, and steady state operation had been achieved.

III.2.1 Simulation Boundary Conditions and Assumptions

For the Comprex® testing, certain assumptions needed to be made with regards to the internal operation of the machine. Endwall-to-rotor clearances were assumed to be 0.0025 in. at the air and exhaust ends. This value comes from the difference in the rotor length and the rotor shroud length. The finite passage wall thickness, which is not

modeled, was assumed to create an 18% blockage effect based on the ratio of wall thickness (0.04") to average passage width (0.221"). The air inlet port, AI was assumed to have a 1% total pressure loss between the measurement station and the face of the rotor where the boundary conditions were imposed. The total temperature imposed was the same as the measured value from upstream. Similarly, but more severely, the exhaust inlet port, EI was assumed to have a 4-6% total pressure loss between the measurement station and the face of the rotor. These losses are reasonable estimates based on the rather convoluted port flow path geometry and the computed Mach numbers of the respective port flows. Clearly however, they will require experimental validation in the future. The air outlet port, AO requires an imposed static pressure at the rotor face. The values imposed at each of the three simulated operating points were adjusted until the ratio of EI to AI mass flow rates matched the experiment. The throat area of the simulated exhaust outlet valve, EO was chosen such that the mass flow at AI matched the experiment for one of the three comparison operating points. It was held at this value for the other operating point comparisons.

At each of the outflow ports (AO and EO), where a static pressure is imposed, a mixing calculation is performed on the integrated limit cycle mass, momentum and energy fluxes. These calculations yield total pressures and temperatures which may be compared to the downstream total conditions measured in the experiment (20). It should be noted, however, that the mixing calculations result in total pressure losses which scale with the degree of non-uniformity in the flow. They do not account for aerodynamic losses associated with the geometry of the ports. Thus it is expected that the total pressure calculated at AO and EO will consistently exceed the experimental

49

measurements which, by virtue of their downstream location, do capture the aerodynamic losses.

III.3 Scaled Pressure Wave Supercharger Design and Simulation Setup

The ultimate goal of this research is to develop a pressure wave supercharger scaled to fit a 95cc Brison engine. To achieve this goal, the scaled PWS had to be designed and then simulated with the validated NASA GRC wave rotor CFD code. The design was accomplished using equations published by Brown Boveri Company in 1983. The simulation required additional changes to the CFD code to account for the decreased size and changes made to the compression cycle.

III.3.1 Scaled Wave Rotor Design

In order to have an operational pressure wave supercharger for a 95cc engine, one must first be designed using the specifications of the Brison engine. Gyarmathy of Brown, Boveri and Company, published the equations used to design the Comprex® in 1983 (16). The use of these equations for the Comprex® CX-93 are shown in Equations 8-11 below.

The rotor dimensions and port placement are key in achieving the proper compression and flow rate. The size of the engine to be supercharged dictates the rough size of the rotor needed to accomplish the compression. The 2.0 liter Mazda diesel engine with the Comprex® CX-93 had a maximum speed of 4200 rpm. According to Gyarmathy (16) at maximum speed, the engine requires a volumetric air flow of 2.47 ft^3/s. The literature shows that the cross sectional area of AO needed to be 10% of the rotor cross sectional area and the rated air speed in the port was 328 ft/s (16). Using

Equations 8 and 9, the required radius was calculated. The calculations result in a

required radius of 1.86 inches for the Comprex® used on the Mazda 2.0 liter diesel

engine

$$A_{AO} = 0.10 * (\pi r^2) \tag{8}$$

$$\dot{V} = A_{AO} * u \tag{9}$$

The Comprex® CX-93 had a length of 3.66 inches. Gyarmathy (16) uses

Equation 10 and an average pressure wave speed of 1312 ft/s, to find the time required

for the wave to travel the length of the rotor. For the CX-93, the time to travel the length

of each passage was calculated to be 0.23 milliseconds. For ideal rotor timing,

Gyarmathy (16) states that each wave typically traveled across the passage nine times per

cycle. Given that there were two cycles per rotation, the rotation time of the rotor was

calculated with Equation 11. This calculation resulted in a rotation time of 4.0

milliseconds. To achieve this rotation time, the rotor needed to spin at approximately

15,000 revolutions per minute. According to Hitomi et al. (10) the Mazda Comprex®

uses a pulley ratio of 4.25:1, indicating that the Comprex® has a design point of around

3,500 RPM engine speed. These same equations were used to design the PWS scaled for

the Brison engine.

$$t = L/a \tag{10}$$

$$T = 2 * t * 9 \tag{11}$$

III.3.2 Scaled Pressure Wave Supercharger Simulation

The simulation of the scaled PWS was accomplished using the same NASA GRC wave rotor code. To simulate the smaller model, changes needed to be made to the program's input file. The program input file contains a number of non-dimensional terms that describe the port size, channel size, rotor length, rotational speed, cycle length, and endwall gap. This file is also where the endwall pockets are simulated. Since all of these parameters are drastically different from the CX-93, they all needed to be recalculated based on the designed parameters of the scaled PWS. The details of the scaled PWS design will be discussed in Chapter IV.

III.4 Uncertainty Analysis

Each experimental measurement taken has an uncertainty in the accuracy of the value returned by the measurement device. These measurement uncertainties compound when they are used in the calculation of a parameter. For this research, the mass flows at AO and EO were calculated using Equation 7 while Equation 4 was used to calculate the mass flow at EI. The mass flow at AI was calculated based on the other three mass flows. The uncertainties of the measurement made by each of the pressure transducers and thermocouples used to calculate the mass flow must be included in the calculation of the mass flow uncertainty. Table 3 shows the manufacturer quoted uncertainties for the instruments used to measure these values.

Table 3: Manufacturer instrument uncertainty

Instrument	Range/Value	Uncertainty
Sonic Nozzle	0.494"	0.0005"
Sonic Nozzle Pressure Transducers	0-100 psi	0.1% Full Scale
Sonic Nozzle Thermocouple	-328 F - 2282 F	4° F
EO Venturi Throat	1.87"	0.02"
EO Differential Transducer	0-5 psi	0.5% Full Scale (0.025 psi)
AO Venturi Throat	0.87"	0.01"
AO Differential Transducer	0-15 psi	0.5% Full Scale (0.075 psi)
Total Pressure Transducers	0-60 psi	0.25% Full Scale (0.15 psi)
Static Pressure Transducers	0-60 psi	0.25% Full Scale (0.15 psi)
Thermocouple	-328 F - 2282 F	4° F

The actual uncertainty present in each mass flow calculation was found using Equation 12 published by Hughes and Hase (29) where α is the uncertainty and Z is the function being used to calculate the parameter of interest.

$$\alpha_Z{}^2 = \left(\frac{\partial Z}{\partial A}\right)^2 (\alpha_A)^2 + \left(\frac{\partial Z}{\partial B}\right)^2 (\alpha_B)^2 + \left(\frac{\partial Z}{\partial C}\right)^2 (\alpha_C)^2 + \cdots \qquad (12)$$

Using Equation 12 and the instrument uncertainties from Table 3, the uncertainties for the calculated mass flows at each port were calculated (Table 4). The uncertainty of the mass flow at AI was calculated using Equation 12 and the uncertainties of the other three mass flows.

Table 4: Mass flow uncertainties

Port	Mass Flow Uncertainty
AO	1.20%
EO	1.90%
EI	0.56%
AI	2.30%

IV. Analysis and Results

This Chapter will discuss the experimental results obtained during the four phases of this research program. The first is to test the Comprex® pressure wave supercharger by simulating engine conditions in the laboratory and recording the mass flows, pressures and temperatures at each port. The second phase is to simulate experimental points using the NASA Glenn Research Center quasi 1-dimensional computational fluid dynamics code and compare the experimental results to those predicted by the simulation to validate the code's ability to predict the Comprex's® pressure gain performance. The third step is to make an initial design of a pressure wave supercharger scaled to fit a 95cc internal combustion engine. The final step is to use the CFD code validated for the Comprex® to predict the performance of the scaled PWS. This chapter will discuss the results found during this investigation and reveal how well the CFD code matched the experimental data as well as discuss the predicted performance of the RPA scaled design.

IV.1 Comprex® Experimental Results

To establish the performance of the Comprex®, two runs were completed at two different speed regimes. These speeds were 2,500 RPM and 3,000 RPM. For each condition the Comprex® was maintained at a constant speed while the opening of the valve on AO was varied to attempt to match the mass flows as described in Chapter III.1. After a value for the valve opening was established based on the mass flows entering and exiting each port, a second run was completed keeping the valve on AO set to a constant value while varying the speed at which the Comprex® rotor was spinning.

54

IV.1.1 2,500 RPM Simulation

To begin testing the performance of the Comprex® CX-93 pressure wave supercharger, laboratory conditions were set to simulate the Mazda 2.0 liter engine operating at 2,500 revolutions per minute. As shown in Chapter III, Table 1, this requires a mass flow of 13.1 lb/min entering the exhaust in (EI) port. Using the Comprex® pulley ratio used in the Mazda 626, published as 4.25:1 (16), this engine speed requires a Comprex® rotor speed of 10,625 RPM.

With the Comprex® running at a constant speed, the opening of the valve on the air out (AO) port was varied thus controlling the mass flow leaving via this port. The valve on AO was varied from 30% to 80% open to observe how the mass flows and pressures changed over the tested range.

After initial experimental runs with the Comprex®, there appeared to be a mass flow continuity issue. The initial experiments indicated that mass was not being conserved when using the established calibration curves discussed in Chapter III to calculate mass flow. The mass flow exiting the Comprex® was less than the mass flow entering the machine. There was an average of 4.5 lb/min more entering the Comprex® than was exiting (Figure 31). This led to the conclusion that one or more of the mass flow measuring devices were in error, so the calibrations of each device was investigated.
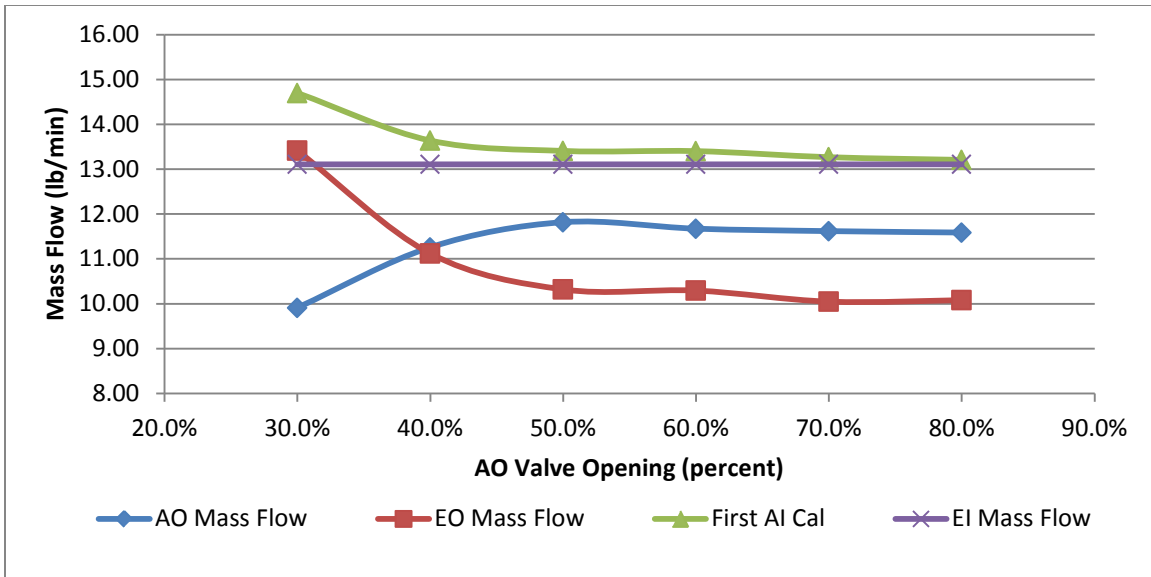
Figure 31: Mass flow with varying AO opening with first mass air flow sensor calibration

The sonic nozzle metering the mass flow to EI was calibrated against national standards, so it was taken to be the standard. This left the venturis at AO and EO and the mass air flow (MAF) sensor on AI. All of these systems were recalibrated in the same manner as discussed in Chapter III. Both venturi calibrations returned results very similar to the original calibration, but the MAF sensor's new calibration was different. These results indicated that a faulty calibration was the reason for the mass flow continuity issue. To verify this assumption, the original raw data was scaled by the new MAF calibration curve (Figure 32). While the excess mass flow was reduced by 1.4 lb/min, the results still did not conserve mass flow as there was still an average excess of 3.1 lb/min. Since the MAF sensor calibration made drastic changes from the first to the second calibration, it was believed that this was the sensor in error. To alleviate the issue, it was assumed that the other three mass flows were correct and mass continuity

was used to solve for the mass flow into AI. This calculated value of AI was used for all the experimental data.
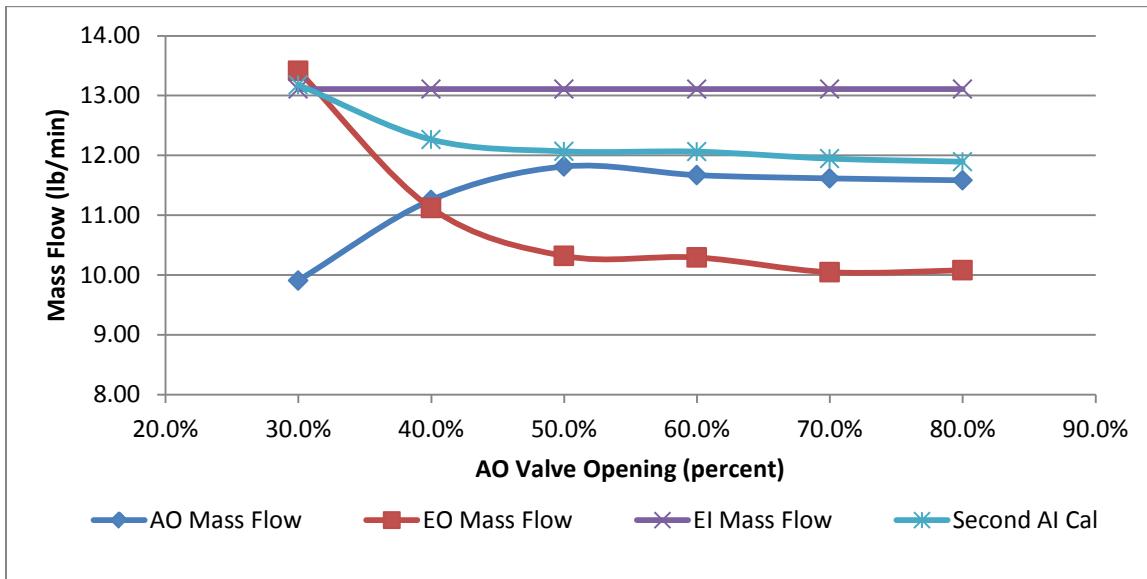
Figure 32: Mass flow with varying AO opening with second mass air flow sensor calibration

With the mass flow discontinuity resolved, the same test was run again using continuity to find the mass flow at AI. The results from the new run are shown in Figure 33. These results show that as the valve at AO was opened, the mass flow exiting AO increased while the mass flow out of EO is decreased indicating that the valve is effectively controlling the exit mass flow at each port. The mass flows at Both EO and AO remain constant once the valve at AO is opened more than 60%. It is suspected that beyond this point, the flow through AO is controlled by the fixed venturi throat rather than the valve opening. Therefore opening the valve further causes no additional change to the mass flows.
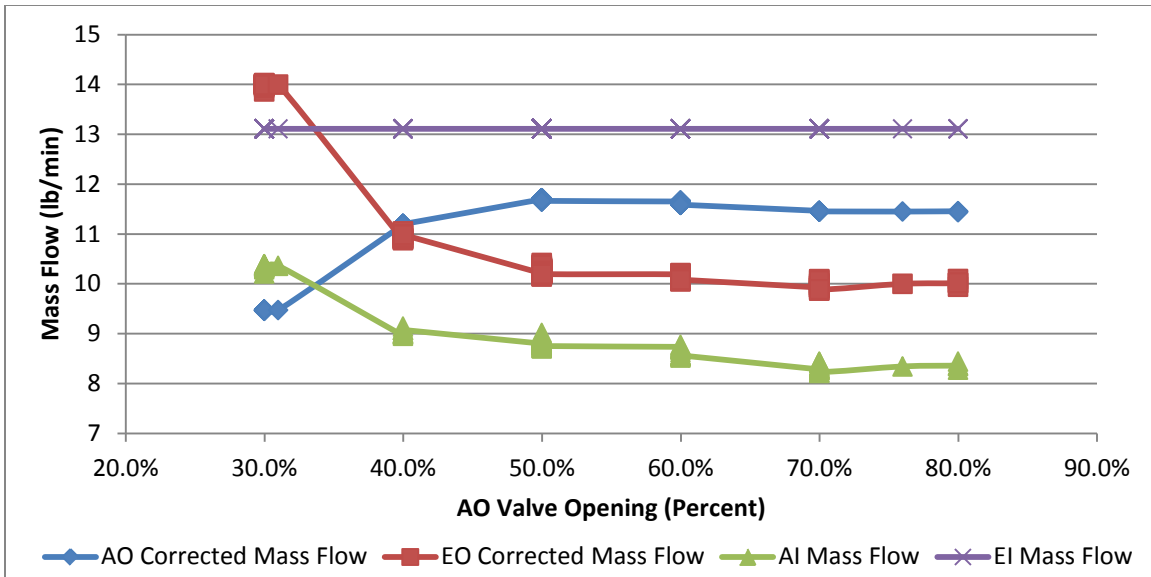
Figure 33: Mass flows with change in AO valve opening; 2,500 RPM simulation

As described in Chapter III, in actual engine operation, the mass flow at AO and EI and the mass flows at AI and EO should be equal with the mass flow at AI and EO being greater than the mass flows at AO and EI. As shown in Figure 33, the mass flow at AO does not equal the mass flow at EI at any point. This is because the temperature of the air introduced at EI was not as hot as actual exhaust temperatures would be. This was later proven with a CFD simulation at a higher temperature. The results of this simulation will be discussed in Chapter IV.2.2. At this mass flow rate, the maximum temperature achievable was 883 R whereas typical diesel exhaust temperatures would be 1460 R. Since the goal of this research was to validate the NASA CFD code for the Comprex®, not completely to replicate the engine conditions, the CFD simulations were run at the actual experimental conditions that existed and the results of the experiments and simulations compared.

Since the operational mass flow matches were not able to be reached, the run point was decided to be at 35% AO open. This point was selected because the mass flows at AI and EO were greater than the mass flows at AO and EI. This mass flow condition indicated that the scavenge air required for proper operation was present thus ensuring the exhaust gases were not ingested into the engine. At the design point selected, AO had a total pressure of 21.52 psi and a mass flow of 10.25 lb/min. For the next run, the mass flow into EI was again set to 13.1 lb/min and the temperature at 883 R. The valve on AO was set to 35% open and the Comprex® speed was varied above and below the nominal operating value of 10,625 RPM. A range of 9,000 RPM to 15,000 RPM was used for the test. Below 9,000 RPM, the Comprex® entered a 'free running' state that will be discussed later in Chapter IV.1.3.
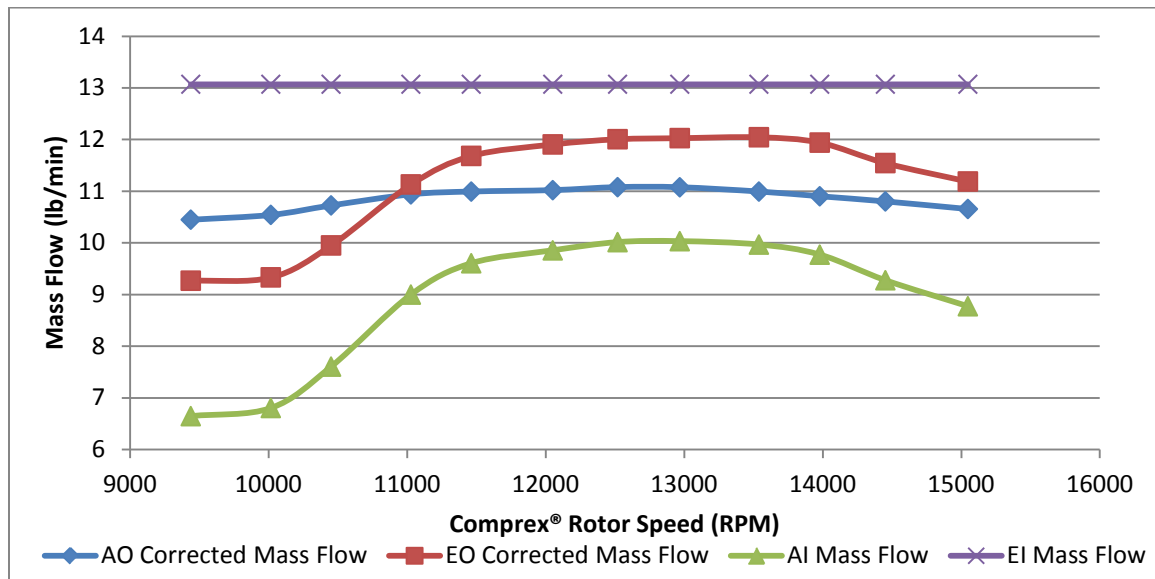

Figure 34: Mass flow with changing Comprex® speed; 2,500 RPM simulation

As shown in Figure 34, the mass flow exiting the air out port (AO) remained constant through a wide range of the Comprex's® speed even as the mass flows at AI and

EO change. This indicated that the endwall pockets were indeed allowing for off design operation without a loss in the mass flow required for the engine to function properly.

Figure 35 shows how the pressure at each port changes as the Comprex® speed is varied. As with the mass flow, the pressure at AO changed very little over the tested range. The consistent pressure supplied to AO was another indication that the endwall pockets were allowing for off design operation while maintaining a consistent pressure boost to the engine.
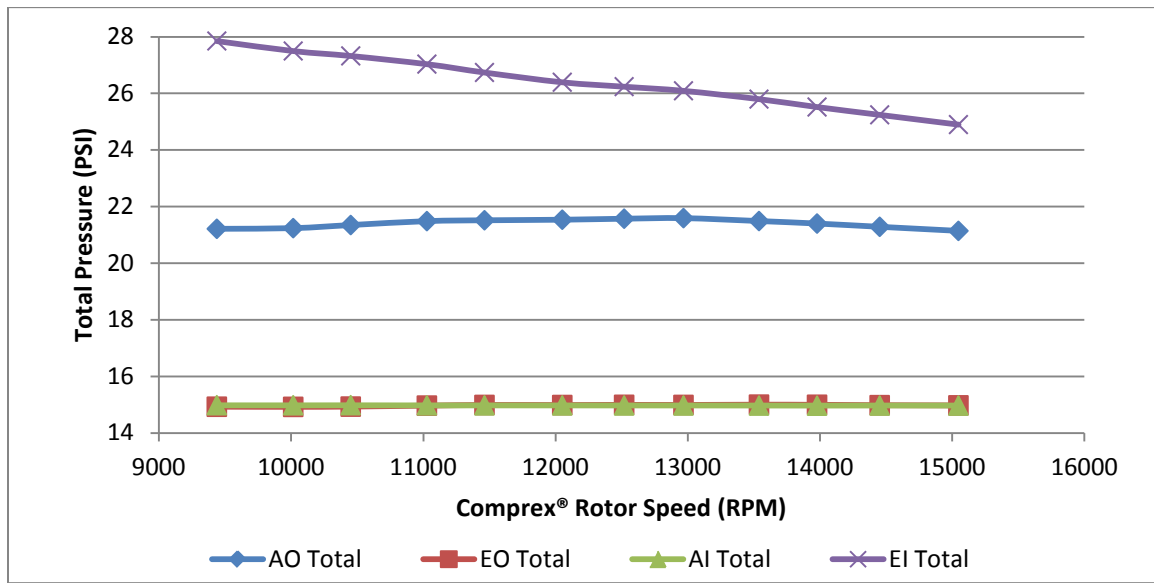
Figure 35: Total pressure with changing Comprex® speed; 2,500 RPM simulation

The average air out pressure across the tested range is 21.4 psi. With an average measured ambient pressure of 14.9 psi, this gives a pressure boost of 1.44 times the ambient air pressure provided to the engine. At the design speed for this exhaust mass flow (10,625 RPM), the pressure at AO (21.5 psi) was directly between the pressure at AI (14.97 psi) and the pressure at EI (27.03 psi). This indicates that, at the design Comprex® rotor speed, the gases completely equalize pressure while in the rotor

60

channels due to the shock wave and the rotor speed being matched at this condition. The ability to continue to provide that pressure above and below the designed speed is solely due to the presence of the endwall pockets.

It is worth noting that the pressure at EO is much less than the pressure of the air exiting via AO. This may cause some concern since the Comprex® is supposed to equalize the pressures. While the pressure at the rotor face would be closer to the pressure at AO, the measurements are made downstream of the rotor face. The pressure at the rotor face quickly approaches atmospheric due to the end of the tube leading from EO being open to the atmosphere. Due to subsonic flow in the EO ducting, the atmospheric pressure at the end of the EO plumbing is communicated to the upstream flow leading to the lower pressure at the measurement location.

IV.1.2 3,000 RPM Simulation

The second test point was to simulate the Mazda engine operating at 3,000 RPM. This required a mass flow into EI of 15.9 lb/min. The maximum temperature obtained at this mass flow was 870 R. This temperature was also significantly below the exhaust temperature seen in actual engine operation. As with the first test, this decreased temperature did not allow for the mass flow matching that would be seen in the actual engine.

For this test point, the first run was to vary the opening of the AO valve to see where the mass flows matched the desired condition of AI and EO being at a higher mass flow than AO and EO. Figure 36 shows how the mass flow at each port varied with the changes in the AO opening. The plot shows that AI and EO are higher than AO and EI at

a little less than 30% open. The ideal run point for the RPM sweep would then be at 28%. When the test was run, the erroneous mass flows from the original mass air flow sensor calibration discussed earlier in this chapter were being used. These mass flows indicated the proper run point to be at 37% open. The run was going to be redone at the proper valve setting, but due to a bearing failure and a long lead time for a replacement unit, this was not able to be completed. The bearing failure will be discussed completely in Chapter IV.1.4. The results that were compiled were consistent with the first test. The wide range of operation demonstrated in the first set of tests and the consistency of this data with the first test indicates that the data was still usable.
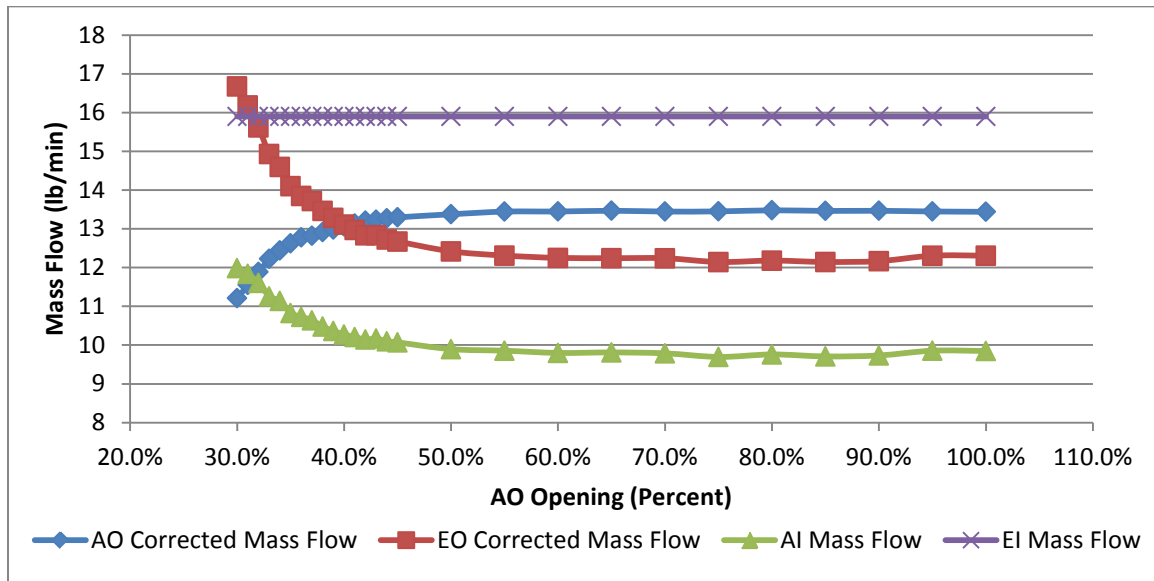

Figure 36: Mass flows with change in AO valve opening; 3,000 RPM simulation

Like in the 2,500 RPM test, Figure 36 shows that beyond 60% valve open, the mass flows at all ports remain constant. Again, this is due to the constriction of the venturi throat limiting the mass flow more than the valve beyond this point. At the

selected operation point of the AO valve open to 37%, the mass flow at AO was 12.8 lb/min and the total pressure was 22.7 psi in the AO valve sweep.

The next run was completed at 15.9 lb/min mass flow into EI at 870 R. The AO valve was set to 37% open. The Comprex® rotor speed was varied above and below the nominal speed of 12,750 RPM from 11,500 to 15,000 RPM. The results, seen in Figure 37, were very similar to the results from the 2,500 engine RPM simulation. The mass flow exiting from the AO port remained constant across the tested range averaging 12.6 lb/min with a low mass flow of 12.3 lb/min and a high mass flow of 12.8 lb/min. This consistent mass flow being provided to the engine once again indicated that the endwall pockets were able to maintain operation across a large rotor speed range.
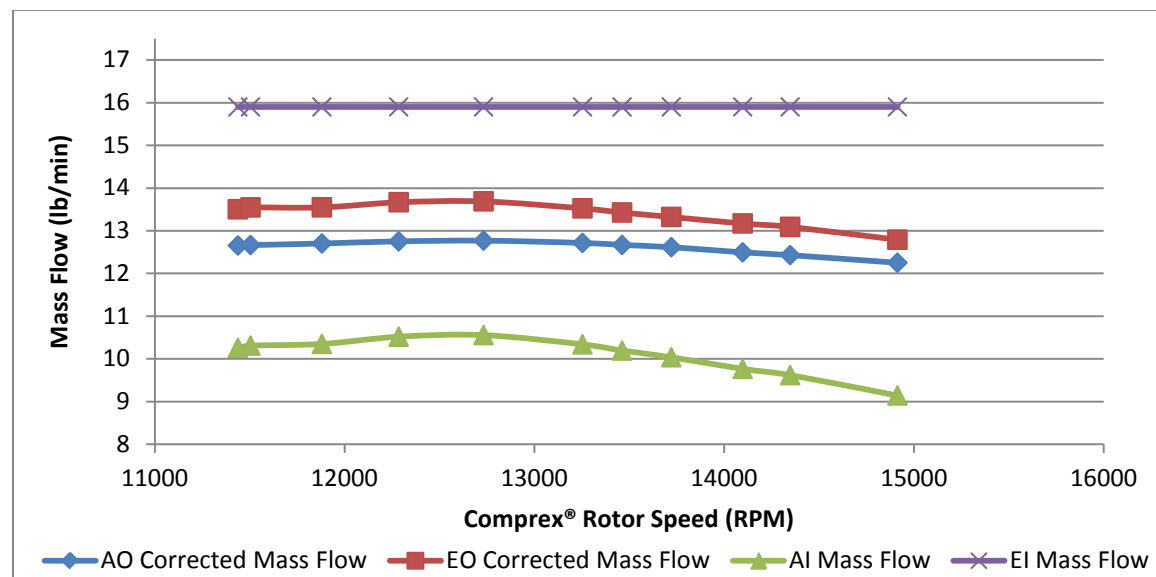

Figure 37: Mass flows with change in Comprex® rotor speed; 3,000 RPM simulation

Figure 38 shows how the total pressures at each port varied as the rotor speed was changed. Like with the 2,500 RPM test, the pressure at AO remained constant across the entire tested range. The air entering the engine maintained a pressure of between 22.2

and 22.7 psi with an average total pressure of 22.6 psi. This led to a pressure boost of

1.49 to 1.52 averaging 1.51 times the ambient air entering the Comprex®. At the

nominal Comprex® rotor speed of 12,750 RPM, the exhaust in pressure was 28.7 psi and

the air in pressure was14.95 psi. The air out pressure of 22.7 psi is very close to the

average of the EI and AI total pressures. These runs again shows that the gases were

given adequate time to completely equalize pressure while in the Comprex® rotor and

proves the Comprex® was able to produce an adequate pressure boost to the engine at off

design mass flows as well as off design temperatures and speeds shown in the 2,500 RPM

test.
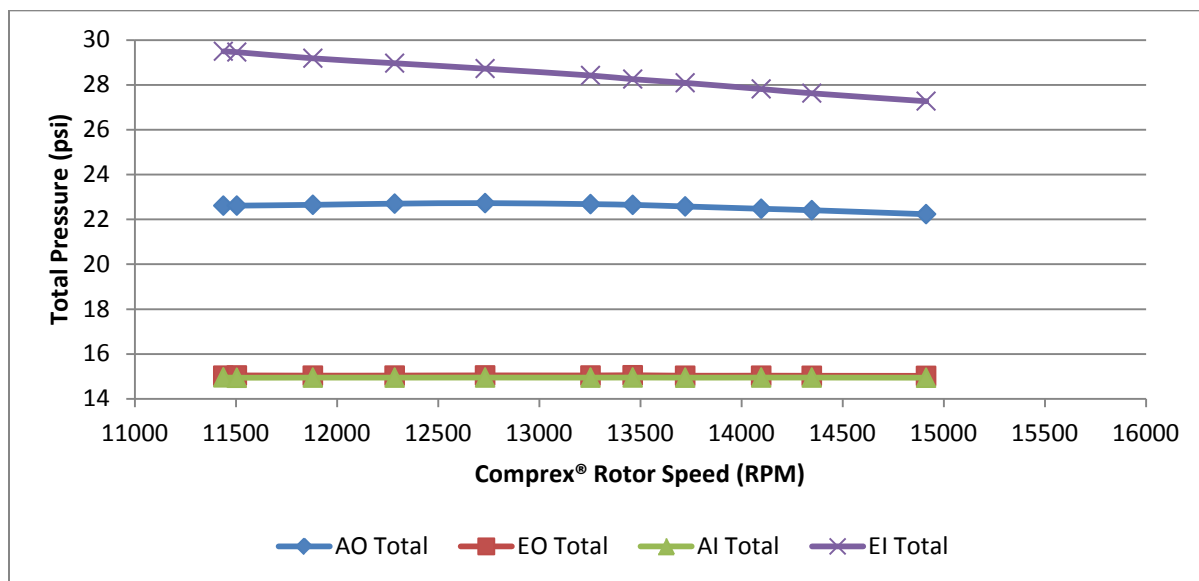
Figure 38: Total pressure with change in Comprex® rotor speed; 3,000 RPM simulation

IV.1.3 Free Running Nature of the Comprex®

        As was discussed in Chapter II, the ports of the air and exhaust in are angled

(Figure 39) to provide a tangential velocity to the air as it enters the rotor. This tangential

velocity provides the force necessary to spin the Comprex® rotor thus limiting the amount of power that is required from the accessory belt driven by the engine. This design aspect gives the Comprex® what is referred to by Zehnder et al. (31) as a "Free Running" nature.

Figure 39: Angled inlet ports on Comprex® pressure wave supercharger

As previously mentioned, the low end of the tested RPM range was limited by the free running nature of the Comprex®. This limit occurred at 9,500 RPM in the simulation of the engine operating at 2,500 RPM and 11,500 RPM in the simulation of the engine operating at 3,000 RPM. At these points, the angled entry of the air and exhaust in ports caused the Comprex® rotor to attempt to spin at a speed much faster than the frequency controller commanded the motor. Therefore, the frequency controller faulted due to a programmed safety feature. Without a drive motor, the Comprex® continued to rotate and reached a steady state rotor speed of 10,900 RPM and 13,600 RPM in the 2,500 RPM and 3,000 RPM simulations respectively.

As with the driven rotor tests, the Comprex® continues to give similar consistently in the pressure of the air output to AO (Figure 40) and a more consistent mass flow for all ports across the RPM range (Figure 41).
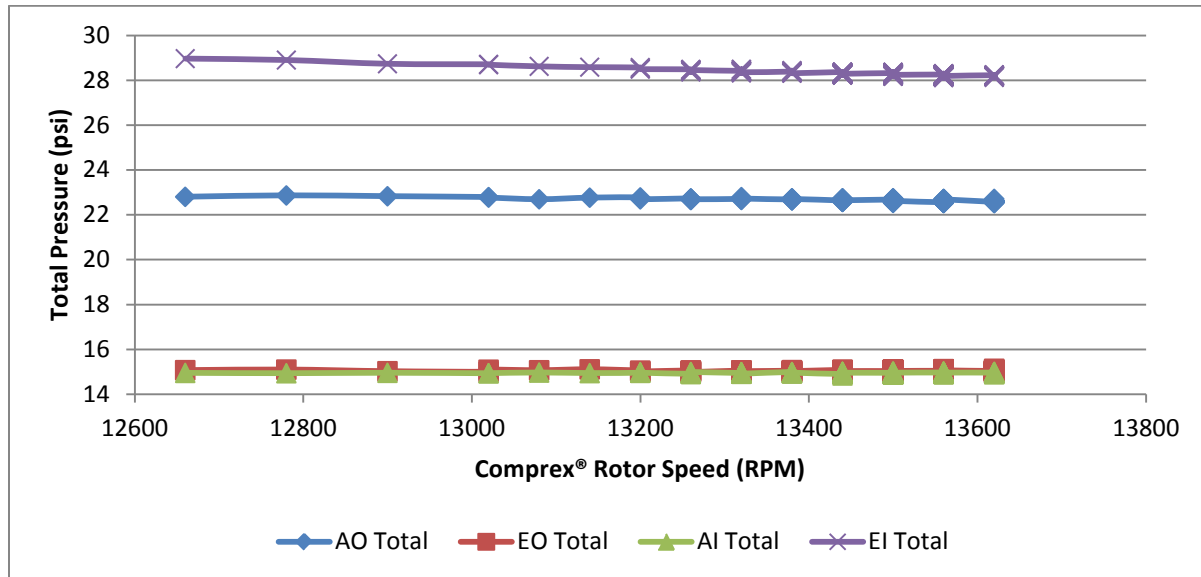
Figure 40: Total pressures in free running Comprex®, 15.9 lb/min at EI
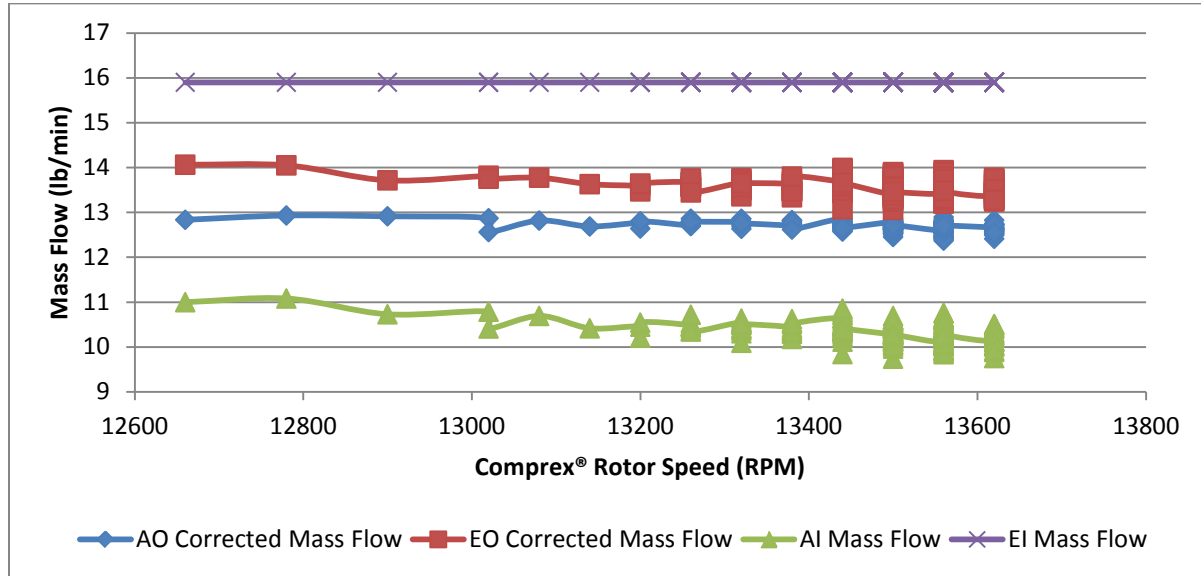
Figure 41: Mass flows in free running Comprex®, 15.9 lb/min at EI

In free running mode, the Comprex® produced a boost of 1.43 times the AI pressure and a total pressure of 21.24 psi in the 2,500 RPM simulation. In the 3,000

engine RPM simulation, a boost of 1.51 times the AI pressure and a total AO pressure of 22.6 psi were recorded. In both cases, these specifications are almost identical to the motor driven cases.

The use of the Comprex® in a free running state was published by Zehnder et al. of Asea Brown Boveri (ABB) in 1989 (31). They concluded that with the metal rotor, the large amount of inertia caused sluggish response when changing between speed regimes. The data collected also indicates this fact. As shown in Figure 42, it takes the Comprex® 135 seconds to reach its steady state speed after beginning to free run from a lower rotor speed. To solve this problem, ABB replaced the metal rotor with one made of extruded silicon nitrate. Changing the rotor to a ceramic material brought with it two main advantages: lower density and lower thermal expansion. The density of the ceramic is 59% less than that of steel. This allowed for a significant weight reduction thus reducing the inertia of the rotor. The reduction in the thermal expansion coefficient allowed for tighter tolerances between the endwalls and the rotor face. This greatly reduced losses due to the leakage between the rotor and the endwalls increasing the overall efficiency (31).
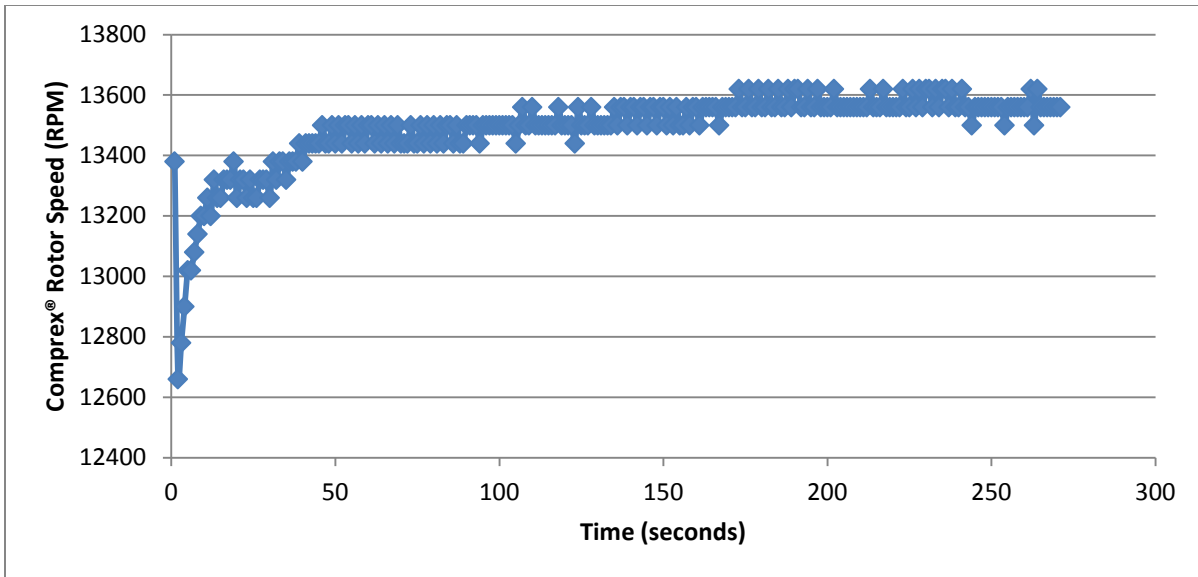
Figure 42: Free running Comprex® response time, 15.9 lb/min at EI

IV.1.4 Rig Failure

In the initial rig setup, the Comprex® was sent to be glass bead blasted to clean the surfaces. During the media blasting, crushed glass got between the seals on the outer Comprex® bearing in the cold endwall. This required the bearing to be replaced. Due to the rarity of the Comprex®, an original equipment replacement was not available, so a bearing was sourced from a local company. A bearing was found that was able to handle the rotational speeds necessary for use in the Comprex® and none of the other given specifications for the bearing gave any indication of incapability with use as a replacement. The bearing was installed and run with cold air flow through the system and gave no indication of problems, so the engine simulation tests were started. After data was taken in the 2,500 engine RPM simulation, the Comprex® was running and suddenly stopped. The initial assumption was that the drive motor had failed, but upon inspection, the Comprex® rotor was seized. The Comprex® was disassembled and the cause of the seizure was discovered: the bearing had completely failed (Figure 43).

Figure 43: Replacement bearing before and after

Further inspection of the Comprex® showed that the bearing failure had sent the rollers through the rotor and caused extensive damage to the walls between the cells as well as damage to the cold endwall (Figure 44).
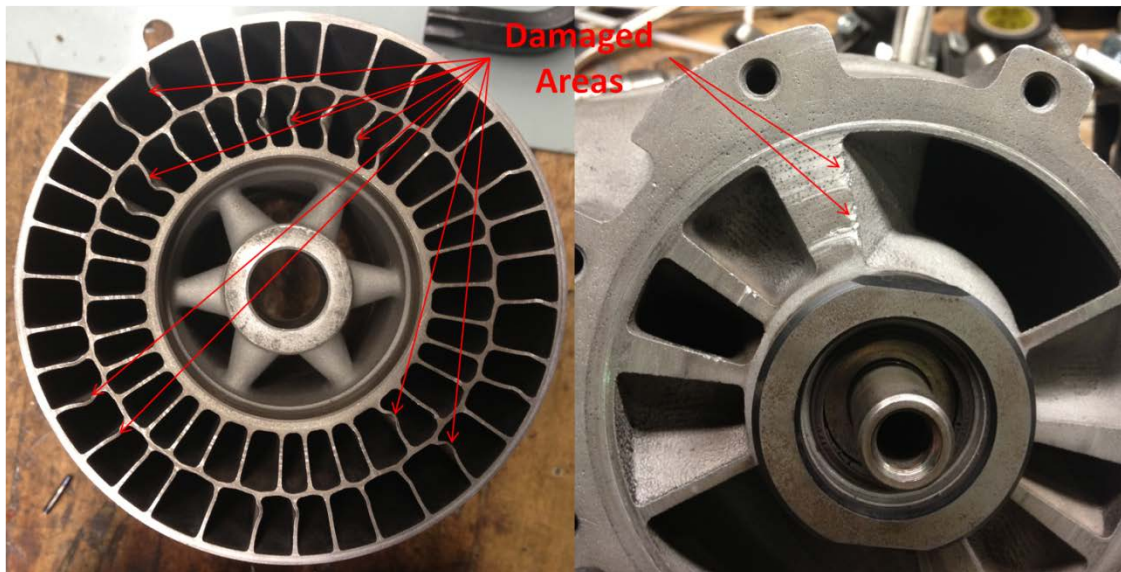
Figure 44: Bearing failure damage

In an attempt to continue the experimentation, the damage to the rotor walls and endwall was repaired by straightening the rotor walls and filing the rotor walls and the endwall to a smooth finish. Thinking that the bearing failure was due to excessive run time, another bearing of the same type that was on hand was used to replace the worn one and the experiments were continued. The 3,000 RPM engine simulation was completed the following day with no noticeable issues. Prior to attempting another engine speed simulation, an attempt was made to spin the Comprex® by hand to ensure the bearing was holding up. The rotor would not spin indicating the bearing had once again failed. The Comprex® was disassembled and a result similar to the first bearing failure was found, but because it was caught before running with the destroyed bearing, the rotor and endwall were not damaged. Since this bearing had only been used for about 5 hours, it was assumed that the run time was not the issue. A closer inspection of the bearing showed that the plastic that held the rollers had melted. This indicated that the bearing failures were due to heat not time.

A bearing able to handle both the rotational speed and heat level in the Comprex® was found and ordered to enable the continuation of testing. The new bearing consisted of ceramic ball bearings and a stainless steel body. Due to the lead time required to get the specialized bearing, it was not received in time to allow for more thorough evaluation.

IV.2 NASA Wave Rotor Code Simulation Results

The experimental measurements provided the required parameters for comparison with the CFD model. Comparison between the two data sets indicated how accurately the mathematical model represented the flow field in the Comprex®. Though the NASA

70

GRC wave rotor code has been used to simulate various wave rotors of different sizes, it has not been validated for the size, geometry, and design elements unique to the Comprex®. The experimentation served as a way to validate the CFD code for this size and type of wave rotor. To validate the code, three of the experimental points representing a wide range of operation were simulated in the CFD code and compared with the experimental results. The points chosen were 13.1 lb/min flow rate into EI at 12,960 RPM rotor speed, 13.1 lb/min flow rate into EI at 9,420 RPM rotor speed, and 15.9 lb/min flow rate into EI at 12,000 RPM rotor speed. These points were simulated with the GRC wave rotor code using the boundary condition procedure described in Chapter III.2.1 and the run conditions from the experiments. The results obtained by the code were then compared to the experimental pressure, temperature, and mass flow at all ports.

Figure 45 shows a series of x-t diagram of the first test case (13.1 lb/min, 12,960 RPM) from the CFD model. The calculated parameters are shown by their respective ports in blue. These diagrams show how the pressure, temperature, and velocity of the air in a single channel of the Comprex® change over one cycle. The colors indicate the relative magnitude of each parameter.
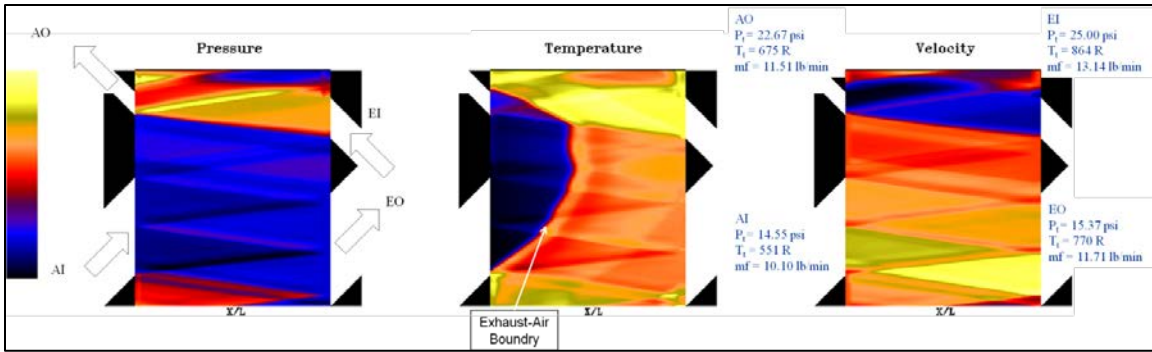
Figure 45: CFD simulation of 13.1 lb/min EI mass flow, 12,960 RPM rotor speed

The temperature diagram clearly shows the separation between the fresh air and the exhaust is maintained throughout the entire compression process. This distinct boundary and the fact that the pocket of air exiting the machine via AO maintains a temperature that is relatively cool when compared to the exhaust entering via EI indicated that there was minimal mixing of the hot exhaust gases with the incoming charge air. This was the desired interaction and representative of what was seen in the experimentation.

From the pressure diagram, it was evident that the air in the Comprex® reaches its highest pressure just as the channel is open to AO. This was also the desired case indicating that the boosted air supplied to the engine inlet was at the highest pressure achieved by the machine during the compression cycle. A look at the relative magnitude of the pressures at EI, AI, and AO indicate that the pressure of the air exiting via AO was directly between the pressure of the exhaust entering EI and the air entering through AI. This was the ideal condition indicating that the gases had completely equalized pressure prior to their exit to the engine. These results also match what was seen in the experiments.

These changes in the pressure and the lack of change in the temperature indicate that the exhaust was not running directly through the machine, but rather compressing the air that has entered through AI prior to being taken to the engine via AO.

IV.2.1 Comparison of CFD Simulation to Experimental Results

The x-t diagram gave good indications that the NASA wave rotor code would accurately predict the performance of the Comprex®. To ensure that the values predicted by the wave rotor code were consistent with the experimental results, the predicted values of the mass flows and pressure and temperature ratios at each port were compared with the experimental results for the three selected test points.

As shown in Table 5, at all three data points used, the mass flows predicted at each point closely mirror those experimentally measured with a maximum difference of 7.55% and an average difference of 2.6%. The low differences between the experimental results and computational predictions indicate that the CFD code is accurately simulating the flow conditions in the Comprex® enabling it to accurately predict the mass flows at each port. Since the mass flows at each port are predicted by the CFD code with only the initial temperatures, pressures and rotor speed, the low error of the mass flow at AI justifies the use of the conservation of mass to calculate the mass flow at this port in the experimental runs.

Table 5: Simulated and experimental mass flow comparison

Mass Flow (lb/min) / Rotor Speed (RPM)	Experimental				Computational				Difference			
	AI	AO	EI	EO	AI	AO	EI	EO	AI	AO	EI	EO
13.1 / 12,960	10.05	11.07	13.04	12.02	10.07	11.48	13.11	11.66	-0.16%	-3.71%	-0.48%	2.98%
13.1 / 9,420	6.45	10.18	13.04	9.31	6.38	10.36	12.84	8.84	1.07%	-1.76%	1.58%	5.09%
15.9 / 12,000	10.03	12.59	15.87	13.31	9.94	11.64	15.76	14.04	0.92%	7.55%	0.66%	-5.48%

The wave rotor code also accurately predicted the temperature and pressure ratios at each port. For these ratios, the total pressure and temperatures at each port were compared with the reference conditions of 14.7 psi and 518 R. Tables 6 and 7 show the correlation between the code generated pressure and temperature ratios with those determined in the experiments. The pressure ratios are predicted with a maximum difference of 14% with an average difference of 4.7%. The temperature ratios are predicted with a maximum difference of 7% and an average difference of 1.3%.

**Table 6: Simulated and experimental pressure ratio comparison**

Mass Flow (lb/min)/ Rotor Speed (RPM)	Experimental				Computational				Difference			
	AI	AO	EI	EO	AI	AO	EI	EO	AI	AO	EI	EO
13.1 / 12,960	1.00	1.47	1.78	1.02	0.99	1.54	1.70	1.05	1.00%	-4.93%	4.23%	-2.51%
13.1 / 9,420	1.00	1.44	1.89	1.02	0.99	1.65	1.82	1.03	1.00%	-13.99%	3.70%	-0.90%
15.9 / 12,000	1.00	1.54	1.98	1.02	0.99	1.75	1.87	1.06	1.00%	-13.55%	5.69%	-3.89%

Table 7: Simulated and experimental temperature ratio comparison

Mass Flow (lb/min) / Rotor Speed (RPM)	Experimental				Computational				Difference			
	AI	AO	EI	EO	AI	AO	EI	EO	AI	AO	EI	EO
13.1 / 12,960	1.06	1.27	1.66	1.46	1.06	1.30	1.66	1.48	0.00%	-1.97%	0.06%	-1.56%
13.1 / 9,420	1.06	1.35	1.67	1.48	1.06	1.45	1.67	1.47	0.00%	-7.57%	0.04%	1.08%
15.9 / 12,000	1.07	1.34	1.63	1.42	1.07	1.37	1.63	1.43	0.00%	-2.58%	0.01%	-1.02%

From the comparison data, it is obvious that the largest differences are between the experimental and computed pressure ratios. This is due to the differences in the location where the measurements are taken in the experiment and where the CFD code makes its predictions. The CFD code predicts the parameters at the exit plane of the rotor. Due to space limitations, the experimental measurements could not be made at this location. The experimental measurements are made downstream of the rotor on the air

and exhaust out ports and upstream of the rotor on the air and exhaust in ports (Figure 46).
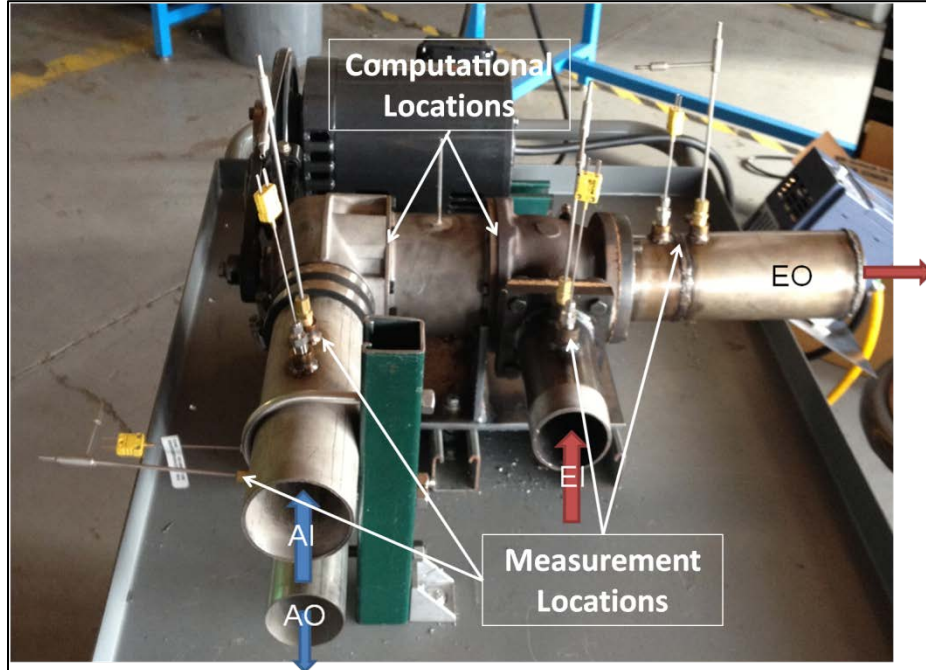
Figure 46: Comparison of CFD prediction and experimental measurement locations

The differences this location offset cause are most evident in the pressure ratios because the aerodynamic losses that occur after exiting the rotor, but prior to reaching the measurement location, are not accounted for. These aerodynamic pressure losses are far greater than the temperature loss between the two locations.

From Table 6 it can be seen that the inlet ports are consistently under predicted by the CFD code while the outlet ports are consistently over predicted. This is likely because the experimental measurements are made prior to the aerodynamic losses on the inlet ports while they are made after the aerodynamic losses occur for the outlet ports.

Table 6 also shows that the largest differences in the experimental results and the computed values occur at AO. This is due to the convoluted path the air has to travel once leaving the rotor along the AO path. As can be seen in Figure 46, the path includes a ninety degree turn just prior to the measurement location. The losses this causes are not accounted for in the CFD code resulting in a large difference in the pressure ratio for this port.

To quantify the aerodynamic pressure losses that occur between the rotor face and the measurement location, the head losses associated with the expansion from the area of the AO port to the tube leading out of the Comprex®, the turns within the Comprex®, and the friction in the pipe at the Comprex® exit were calculated. Fox and McDonald (32) provide Equation 13 to calculate the head loss due to expansion where K_e is the expansion loss coefficient and V_1 is the velocity before the expansion.

$$h_{l,m} = K_e \left(\frac{\bar{V}_1^2}{2} \right)$$ (13)

The expansion loss coefficient is based on the area ratio. For the AO port of the Comprex®, the area ratio was found to be 0.24. This corresponded to a K_e value of 0.44. The velocity in the port was found by using Equation 14 where the mass flow (ṁ) is equal to half the total mass flow measured at AO, ρ is the density and A is the area of the AO port.

$$V = \frac{\dot{m}}{\rho A}$$ (14)

The losses due to turning in the Comprex® can be calculated with Equation 15, where L_e/D is the equivalent length for each turn, V is the velocity and f is the friction factor.

$$h_{l,m} = f \left(\frac{L_e}{D}\right) \left(\frac{V^2}{2}\right) \tag{15}$$

The friction factor was found to be 0.0172. The equivalent length was found to be 46 based on a 90° turn and a 45° turn in the Comprex® flow. The head loss for the pipe at the Comprex® exit was calculated using Equation 16 where L is the length of pipe and D is the diameter of the pipe.

$$h_l = f \left(\frac{L}{D}\right) \left(\frac{V^2}{2}\right) \tag{16}$$

The friction factor was found to be 0.029 and the length was six inches. This gave an L/D ratio of 3. The velocity was calculated using Equation 14, but used the full value for the mass flow and the area of the 2" pipe that is used at the Comprex® exit.

Taking the sum of Equations 13, 15 and 16 gave the total head loss in the path between the rotor face and the measurement location. Using Equation 17, this total head loss was correlated to a change in pressure.

$$\Delta P = \frac{h_{l,total}}{\rho} \tag{17}$$

For the Comprex®, the average total pressure change was found to be 1.88 psi. The 1.88 psi is 8.8% of the total pressure at the exit of AO. Deducting the 8.8% in aerodynamic pressure losses from the pressure differences seen in Table 6 leaves a maximum pressure difference of 5.2% and an average difference of 4.6%

77

IV.2.2 Temperature Aided Simulation Results

In the experimental results, the fact that the mass flows at AO and EI could not be matched, as would be in engine operation, was claimed to be due to the temperature of the gas entering EI not being as high as would be seen in actual engine conditions.   In an attempt to see if this proved to be correct, a CFD simulation was completed using the same operating conditions that were shown for the first test point (13.1 lb/min in EI and 12,960 RPM Comprex® rotor speed) except the temperature of the gas entering EO was elevated. The results, shown in Figure 47, indicate that the lack of heat in the exhaust surrogate was the cause of the mass flow mismatch.

The simulation was run by increasing the temperature of the gas entering via EI until the mass flows at AO and EI matched as well as the mass flows at AI and EO as they would in actual engine operation. This condition was achieved at 988 R (still low for a diesel engine exhaust). The mass flow at EO and AI were also higher than the mass flows at AO and EO as is required for scavenge air for the Comprex®.   The pressure of the air leaving AO was also increased by 7.3% resulting in a pressure boost of 1.67 times the atmospheric air compared with the 1.43times boost that occurred under experimental conditions. This indicates that if the representative enthalpies could be achieved in the laboratory equipment, the actual Comprex®-engine operating environment could be replicated.
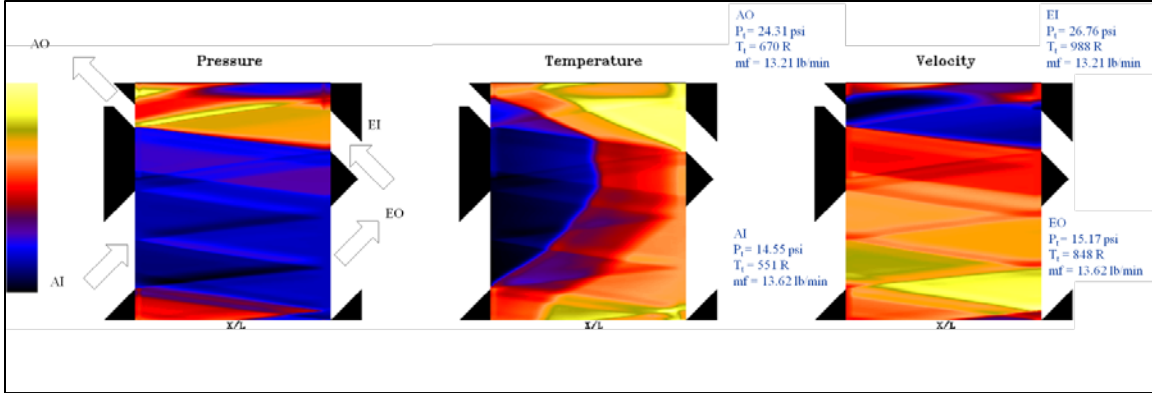
**Figure 47: Temperature aided CFD simulation of test point one**

IV.4 Scale Design

After the baseline performance of the Comprex® wave rotor supercharger had been established and its performance accurately predicted by the NASA GRC wave rotor code, a second wave rotor was designed to match the RPA engine being studied. To begin the design, it is assumed that the waves in the scaled supercharger will look similar to those of the full sized Comprex®. With this assumption, the endplate port timing (size when measured in degrees) for the scaled system remained the same. The physical port size needed was smaller, but the amount of rotation a cell was open to each port remained the same. Due to size constraints when making the system smaller, the number of ports in each endplate was reduced to one inlet and one outlet. This resulted in the system having one cycle per revolution as opposed to two as in the full size Comprex®. The double row of cells used in the Comprex® rotor was replaced with a single row. This allowed for each cell to be larger in an effort to minimize the cell area lost to the boundary layer in each channel.

The required volumetric flow rate of a naturally aspirated 95cc Brison engine was calculated to be 0.39 ft^3/s when operating at 7000 RPM using Equation 7 from Chapter

III. Accounting for the supercharging of the air to 1.5 times the atmospheric pressure when it enters the engine, the supercharged 95cc engine will require 0.59 ft^3/s. Using Equations 1 and 2 from Chapter III, the required area of the rotor was found to be 2.56 in^2 this gave a rotor diameter of 1.81 inches.

Using this data, the scaled rotor was designed to have a single row of 24 cells as opposed to the two rows of 34 cells each used in the Comprex®. The inner diameter of the cells is 1 inch and the outer diameter 1.75 inches. In order to maintain the mean radius to length ratio present in the Comprex® of 0.592, the length was designed to be 1.8 inches. A CAD drawing of the scaled design is shown in Figure 48. These dimensions are similar to those of the wave rotor designed by Okamoto and Nagashima at the University of Tokyo (17) discussed in Chapter II.5. This size similarity indicates that the design is feasible and worth pursuing.
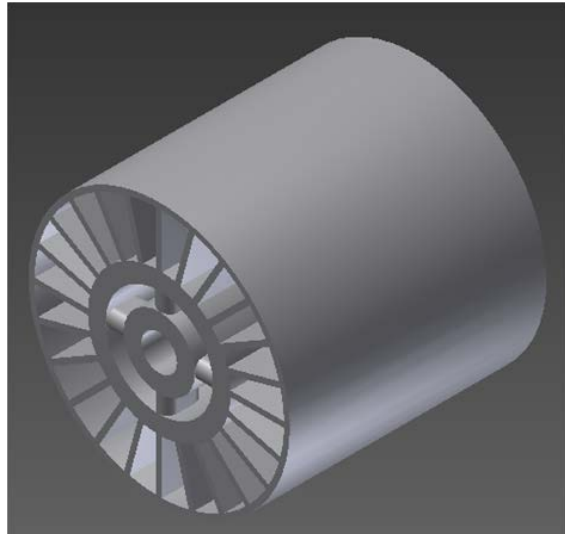
Figure 48: Drawing of scaled rotor

As shown in Figure 49, the scaled rotor is significantly smaller than the original

Comprex® rotor. The scaled version represents an 89% reduction in rotor volume from

the original Comprex®. The design decision to go to a single row of 24 cells as opposed

to the original design of two rows with 34 cells in each allowed for a reduction of only

37% in the cross sectional area of each cell.
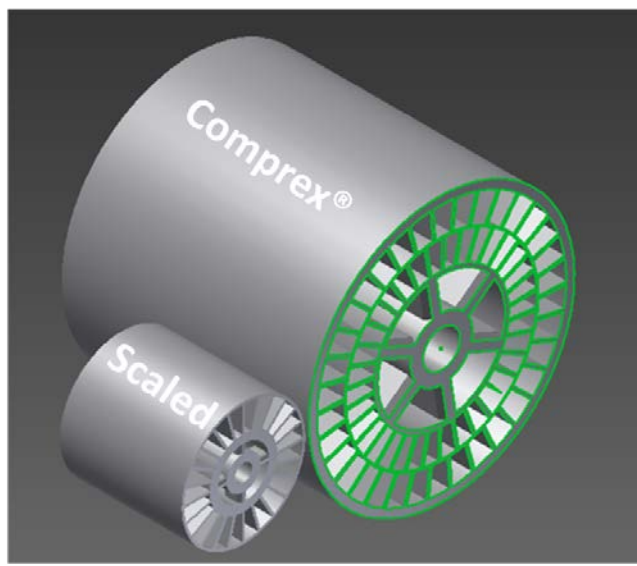
Figure 49: Size comparison of Comprex® and scaled rotor

For the designed size, the estimated rotational speed was calculated using

Equations 3 and 4 from Chapter II. Assuming the speed of sound to be 1312 ft/sec, the

scaled supercharger needed to spin at 30,666 RPM. At an engine speed of 7,000 RPM,

this required a pulley ratio of 4.38:1.

The design of the endwalls of the scaled pressure wave supercharger (Figure 50)

closely follows the design of the Comprex® endwalls. Like the Comprex® being used

on the Mazda diesel engine, the scaled PWS operating on the Brison engine will require

robust off design performance ability. To allow this, the endwalls for the scaled PWS

were designed with pockets similar to those in the Comprex®. Like with the port locations, the pockets were placed in the same radial locations as in the full size Comprex®. Also like the Comprex®, the inlet ports (AI and EI) were angled to eliminate as much of the demand on the engine as possible in turning the rotor. One change that was made from the original Comprex® design was the reduction to one cycle per revolution as opposed to the two cycles per revolution used in the Comprex®. This choice was made due to the reduced space in the smaller endwalls.
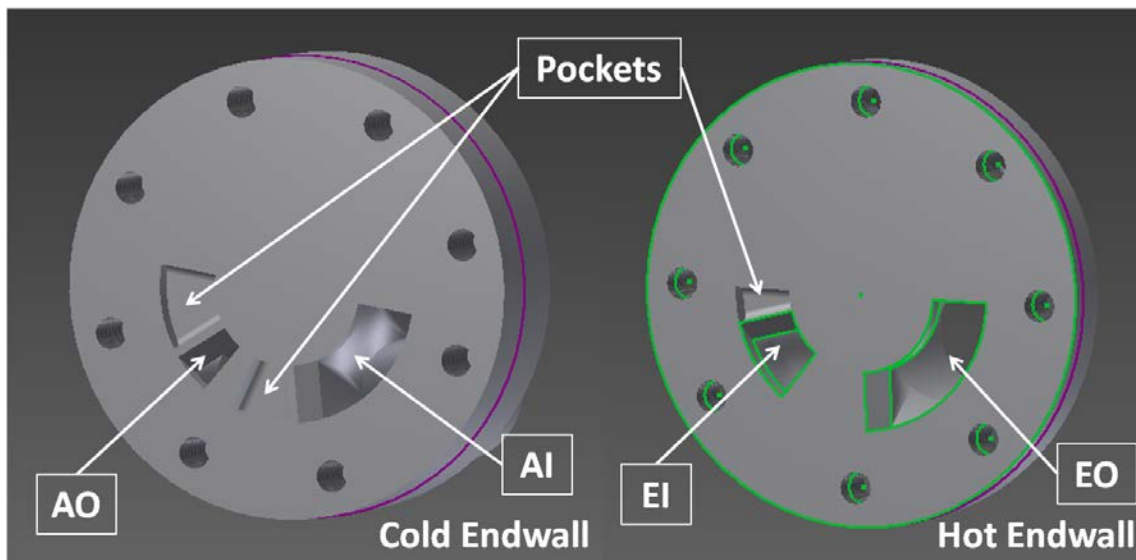
Figure 50: Scaled PWS endwalls

IV.5 Scaled Pressure Wave Supercharger Simulation Results

With the scaled pressure wave supercharger designed, the last step of the research was started: simulate the scaled PWS to predict the performance. Using the modified input file discussed in Chapter III.3.2, the NASA GRC wave rotor simulation was run with an input rotor speed of 30,666 RPM and an initial EI temperature of 1352 R. This temperature is consistent with the exhaust temperatures of the Brison engine published by

Crosbie (2). Figure 51 shows the x-t diagram of the simulation. The simulation shows a complete revolution as opposed to those shown for the full scale Comprex® that showed only a full cycle (half a revolution).
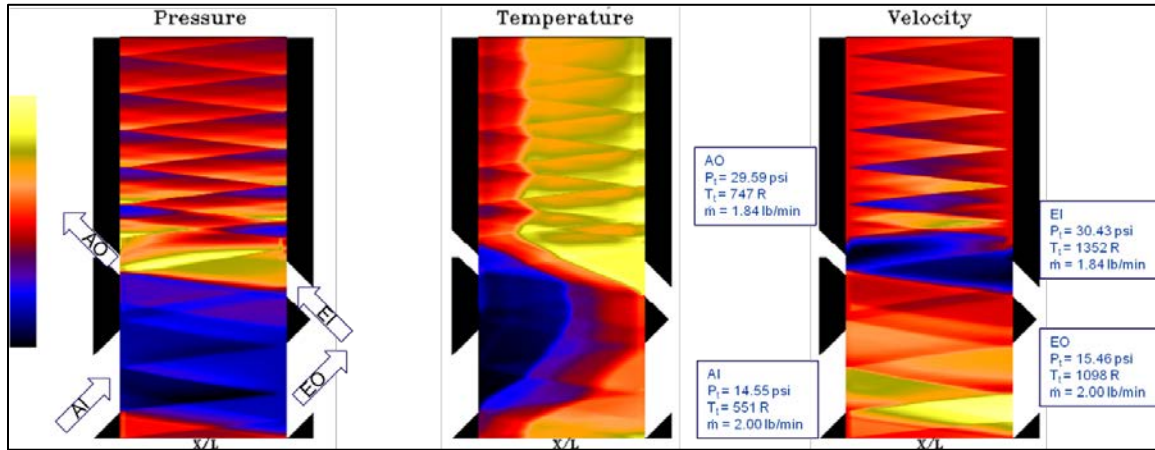

Figure 51: Scale PWS CFD simulated x-t diagram

The x-t diagram shows the distinct division between the inlet air and the exhaust while in the channels like in the full scale simulation. This is best seen in the temperature plot. Also like the full scale simulation, the pressure of the air exiting via AO is at its maximum pressure as it exits the port. This again is the ideal case since it provides the maximum pressure boost to the air to be used by the engine. These parameters indicate the scaled pressure wave supercharger is functioning properly.

The scaled PWS is able to provide air to the engine at 29.59 PSI. This is a boost of 2.01 times the atmospheric pressure. While the expectation was for a decrease in performance when the pressure wave supercharger was scaled, this is a larger boost than was seen in the experimental results. This result may seem as if the machine gets more efficient as its size is decreased, but that is not the case. The scaled pressure wave supercharger is operating exactly at its design point. Due to speed limitations of the

83

electric motor and the heat capacity of the heaters used to simulate the engine exhaust, the design point of a 3,500 RPM engine speed was not obtainable for the Comprex® experiments. When simulated at the design point, shown in Figure 52, the Comprex® was able to provide air to the engine at 35.31 PSI. This represents a boost of 2.4 times the atmospheric air pressure. This shows that the scaled PWS operating on design does not provide as much boost as the Comprex® at its design point. The pressure boost supplied by the scaled PWS represents a 16% loss of pressure gain when compared to the full size Comprex®.
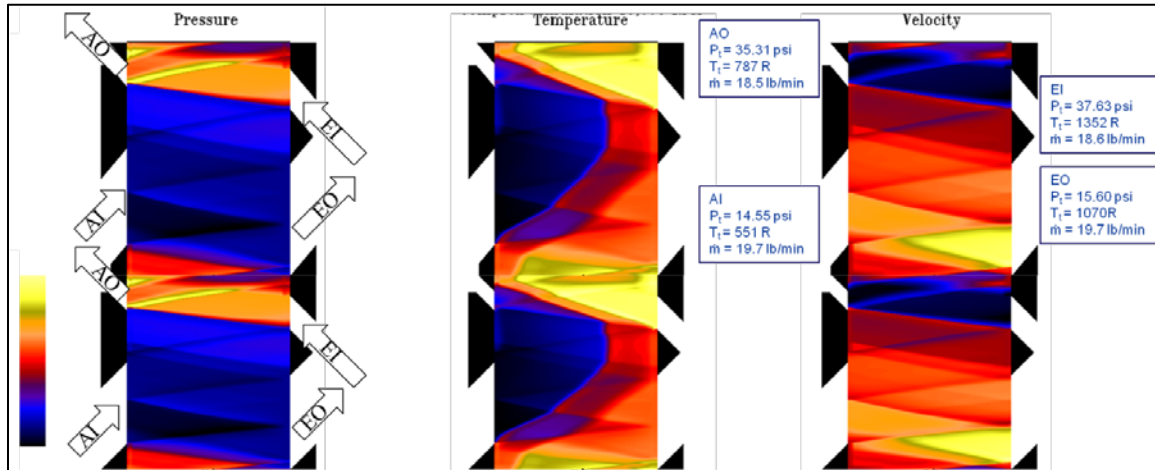
Figure 52: Comprex® simulation at design point

Figure 52 shows a complete revolution (2 cycles) of the Comprex® operating at its design point. By comparing the wave structure of the Comprex® in Figure 51 with that of the scaled PWS in Figure 50 the similarity of their wave structure during the cycle is easily seen. This indicated that the design assumption that the scaled PWS would have a similar wave structure to that in the full sized Comprex® was valid and thus the design decision made based on that assumption were correct.

The simulation of the scaled PWS did highlight a flaw in the design. The CFD code predicts a mass flow of 1.84 lb/min exiting the PWS at AO and going to the engine. The mass flow computed from the volumetric flow required by the Brison engine was 3.9 lb/min indicating that this machine is too small to handle the mass flow requirements of the Brison engine. Since the scaled PWS was designed using the equations published by BBC, the equations were closely examined. For reference, Equation 8 will be presented again as Equation 18.

$$A_{AO} = 0.10 * (\pi r^2) \tag{18}$$

Equation 18 comes from Gyarmathy's assertion (16) that the area of the AO port should be equal to 10% of the total rotor area. Examining the size of the AO port in the Comprex® shows that the port opening in the endwall is 18°. This represents only 5% of the rotor area. This indicates that the 10% of the rotor area comes from the sum of the two AO ports present per rotation of the Comprex® rotor. This would mean that when designing a pressure wave supercharger with only one cycle per revolution, the area of the AO port should only account for 5% of the total rotor area. Using this assumption, in order for scaled PWS to support Brison engine on one cycle per revolution, the diameter of the rotor would need to be 2.56 inches vice the 1.8 inch diameter of the rotor being simulated here.

There are two ways to remedy this design flaw. The first would be to change the diameter of the rotor to 2.56 inches as described above. This would result in a 300% increase in the rotor volume over the current design. The increase in rotor diameter would necessitate an increase in the endwall size as well. These size increases would

85

also result in a large increase in the weight of the machine. Since this pressure wave supercharger is being designed for use on small remotely piloted aircraft, an increase in weight was not desirable. The second option would be to return to two cycles per revolution for the scaled pressure wave supercharger. While fitting a second cycle into each endwall required some design challenges, it allows for the retention of the small size and thus small weight of the current design.

In order to fit the second cycle into each endwall, each pocket had to be resized. Each pocket was decreased in size by 5 degrees. This size decrease allowed for all the ports to retain their initial size as well as the slanted inlets that allow for the PWS to free run. The scaled PWS endwalls with two cycles per revolution can be seen in Figure 53.
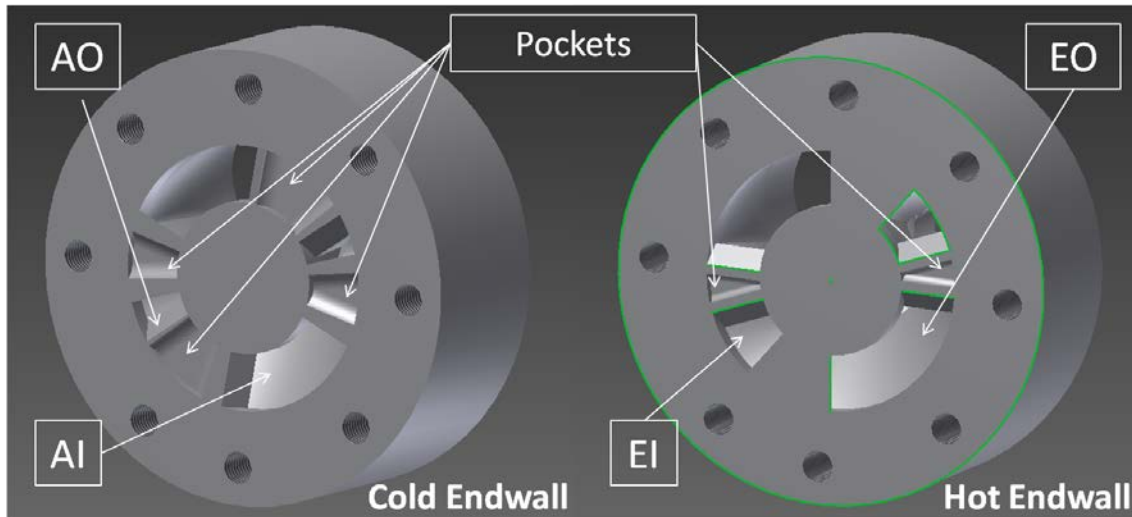
Figure 53: Scaled endwalls with two cycles per revolution

The decreased pocket size is not expected to affect the overall performance of the scaled PWS when used on an RPA engine. The pockets are to provide off-design performance. Since many of the small RPAs are used in long loiter type missions, they will spend most of their operational time at a designed engine speed. The scaled PWS

can be designed at this operating point to ensure the PWS is always operating at its design point.

Though the PWS simulated will not work for the Brison engine, it does indicate that the intent of this research is feasible: a pressure wave supercharger can be scaled for use on small RPA engines. Since the simulated PWS is actually smaller than would be used on a 95cc engine, the pressure boost provided from this machine proves the concept is feasible.

V. Conclusions and Recommendations

V.1 Problem Statement and Objectives

The primary purpose of this research was to increase the reliability and performance of small internal combustion engines used in many of the small remotely piloted aircraft currently being employed by all branches of the Armed Forces. The manufacturers of these aircraft source engines that were intended to be used by radio controlled aircraft hobbyist and lawn care implements since these areas provide inexpensive and readily available options as power plants. Since the original design of these engines was for use at or near sea level and not at varying altitudes, the ability to operate and remain reliable at dynamically changing altitudes was never a design consideration. While the cost and ease of access make these engines excellent candidates to meet the fast acquisition schedules of the military, the lack of performance and reliability at changing altitudes means they are not able to perform as designed when being used as the power plant of a RPA.

In an attempt to alleviate the performance and reliability issues of commercial off the shelf (COTS) engines at altitudes where they were designed to be operated, this research focused on the turbo-normalization of the engines with a pressure wave supercharger. This process would allow the engine to receive an inlet air pressure consistent with sea level conditions while flying at the operational altitudes required for the military use of the RPAs.

To achieve the primary goal of this research, a pressure wave supercharger similar to the Comprex® PWS used successfully on many diesel engines, was designed and

scaled to fit a 95cc Brison two-stroke internal combustion engine. The milestones for

achieving this overall goal were to:

1. Characterize the Comprex® CX-93 performance using laboratory equipment
to simulate the actual engine operating conditions.

2. Use the NASA Glenn Research Center quasi 1-dimensional wave rotor
computational fluid dynamic code to simulate the Comprex® at the experimental
running conditions and compare the CFD predicted pressures, temperatures, and
mass flows at each of the Comprex® ports with those measured in the
experiments to validate that the code accurately predicts the Comprex®'s
performance.

3. Design a pressure wave supercharger similar to the Comprex®, but scaled to
fit a 95cc Brison engine using published equations.

4. Simulate the scaled PWS in the now validated NASA GRC wave rotor code to
predict the performance that could be expected from the scaled PWS.

V.2 Results of Research

The initial step was to simulate the Comprex® running environment using

laboratory equipment. This was accomplished with the discrepancies described in

Chapter III. The experimental conditions were then simulated in the NASA GRC CFD

code and the resulting pressures, temperatures, and mass flows were compared with those

measured during the experimental runs. The CFD predictions closely matched the

experimental results at all ports for all three tested conditions. This correlation between

89

simulated and experimental results demonstrated the wave rotor code's ability to accurately predict the flow conditions inside the Comprex® thus validating the NASA GRC wave rotor code as a viable tool in predicting the performance of Comprex®-like devices.

For the next phase of this research, a scaled pressure wave supercharger to fit a 95cc Brison engine was designed using equations published by Brown Boveri Company. The equations lead to a rotor diameter of 1.8" and a length of 1.85". This represented an 89% decrease in the rotor volume when compared to the original Comprex® CX-93 used in experimentation. The scaled PWS was also designed with a single row of 24 channels as opposed to the original Comprex®'s double row of 34 channels each. This was to prevent the channels from becoming so small that the boundary layer completely closed off the channel.

V.3 Conclusions

The intent of this research was to test the feasibility of using a wave rotor pressure wave supercharger to turbo normalize the air entering the small internal combustion engines used in many of today's remotely piloted aircraft. The scaling study has shown through simulation with the NASA Glenn Research Center wave rotor computational fluid dynamic code that a pressure wave supercharger scaled to fit a 95cc Brison engine will enable the turbo normalization of the air entering the engine. Though there was some evidence of scaling losses with the scaled PWS, it was predicted to provide air at more than two times atmospheric pressure to the engine. This boost in air pressure would allow a remotely piloted aircraft to operate at 18,000 feet and have air supplied to the

engine at sea level pressure. The ability to retain the sea level performance and reliability at 18,000 feet will prove invaluable to all military branches currently employing small remotely piloted aircraft.

V.4 Recommendations

The test rig designed and used for this research proved effective at the gathering of the required data to accomplish the research objectives. There are a few areas in which the test rig could be improved. The first is to find a way to increase the heat to the compressed air used to simulate the exhaust. This could be aided through the installation of insulation on all the pipes leading to the rig from the heaters. The addition of insulation will still not allow for temperatures consistent with actual exhaust temperatures due to the ability of the heaters to heat the air at the required flow rates. In order to obtain actual engine exhaust temperatures, a third heater would need to be added. Another possible solution would be the addition of a hydrogen vitiator to supplement the heat provided by the two existing heaters.

The second improvement needed for the test rig is a reliable mass flow measuring device for the air in port. This could be either a new mass air flow sensor or a third venturi. The venturis proved effective on both of the other ports on which they were used.

The third improvement would be to find a way to increase the top speed the Comprex® rotor can be spun. This could be accomplished with either a new motor capable of a higher speed or replacing the 8.1" pulley currently being used with a larger

91

one. A larger pulley will require some minor modifications to the motor mounting system, but they would be easily accomplished. Increasing the rotor speed will also be necessary to bench test the scaled PWS since its rotational speed is twice as fast as the Comprex®.

V.5 Future Research

While the completed research proved that a pressure wave supercharger scaled to fit an engine consistent with those used on small remotely piloted aircraft can be used to turbo-normalize the air entering the engine, it left many more steps to see the ultimate goal realized. These steps include:

1. Use the new 2 cycle per revolution design to complete more simulations to include off design conditions to ensure the scaled pressure wave supercharger is as robust as the original Comprex®.

2. Once a robust design has been found, a prototype of the scaled pressure wave supercharge needs to be built and bench tested in a manner similar to the experimental tests performed for this research.

3. The final goal would be to fit the prototype to an engine in the 95cc class and test its actual performance.

Bibliography

1.) Schmick, P. (2011). <u>Effects of Atmospheric Pressure and Temperature on a Small Spark Ignition Internal Combustion Engines' Performance</u>. AFIT Thesis. AFIT/GSE/ENY/11-M28 Air Force Institute of Technology, Wright-Patterson AFB, OH.

2.) Crosbie, S. (2012). <u>Increasing Reliability of a Small 2-Stroke Internal Combustion Engine for Dynamically Changing Altitudes.</u> AFIT Thesis. AFIT/GSE/ENY/12-M08 Air Force Institute of Technology, Wright-Patterson AFB, OH.

3.) Weber, Helmut E., *Shock Wave Engine Design*, 1st ed., John Wiley & Sons, New York, 1995, Chaps. 5, 6.

4.) Knauff, R., 1906, "Converting Pressures of Liberated Gas Energy into Mechanical Work," British Patent 2818.

5.) Burghard, H., 1913, British Patent 19421.

6.) Lebre, A. F., 1928, British Patent 290669.

7.) Akbari, P., Nalim, M.R., Müller, N., "A Review of Wave Rotor Technology and its Applications," Journal of Engineering for Gas Turbines and Power, Vol 128, Pages 717-735, October 2006.

8.) Kentfield, John A.C., *Nonsteady, One-Dimensional, Internal, Compressible Flows Theory and Applications*, 1st ed., Oxford University Press, Inc., New York, 1993, Chap. 7.

9.) Iancu, Florin, Piechna, Janusz, Müller, Norbert, "Basic Design Scheme for Wave Rotors," Shock Waves, vol 18, pp 365-378, 2008.

10.) Hitomi, M., Yuzuriha, Y., Tanaka, K., "The Characteristics of Pressure Wave Supercharged Small Diesel Engine," SAE Technical Paper 890454, International Congress and Exposition, Detroit, Michigan, Feb 27 – Mar 3, 1989.

11.) Hirecaga, M., Iancu, F., Muller, N., "Wave Rotors Technology and Applications," Scientific Bulletin of the "Politehnica" University of Timisoara Transactions on Mechanics Special Issue, The 11th International Conference on Vibration Engineering, Timisoara, Romania, September 27-30, 2005.

12.) Doerfler, P.K., 1975, "Comprex® Supercharging of Vehicle Diesel Engines" SAE Paper 750335.

13.) Zehnder, G. and Mayer, A., "Comprex® Pressure-Wave Supercharging for Automotive Diesels-State-of-the-Art," SAE Technical Paper 840132, 1984, doi: 10.4271/840132.

14.) Guzzella, L., and Martin, R., "The Save Engine Concept," MTZ Report 10, pp. 9–12, 1998.

15.) Heisler, H., *Advanced Engine Technology*, 1st ed., Arnold, London, 1997, Chap. 6.

16.) Gyarmathy, G., "How Does a Comprex® Pressure-Wave Supercharger Work?," SAE Technical Paper 830234, International Congress and Exposition, Detroit, Michigan, Feb 28 – Mar 4, 1983.

17.) Okamoto, K., Nagashima, T., "Simple Numerical Modeling for Gasdynamic Design of Wave Rotors," Journal of Propulsion and Power, Vol 23, No. 1, Pages 99-107, January-February 2007.

18.) Iancu, F., Akbari, P., Muller, N., "Feasibility Study of Integrating Four-Port Wave Rotors into Ultra-Micro Gas Turbines (UμGT)," AIAA 2004-3581, 40th AIAA/ASME/SAE/ASEE Joint Propulsion Conference and Exhibit, Fort Lauderdale, Florida, July 11-14, 2004.

19.) Wilson, J., Paxson, D. E., "Wave Rotor Optimizing for Gas Turbine Engine Topping Cycles," Journal of Propulsion and Power, Vol 12, No. 4, Pages 778-785, July-August 1996.

20.) Paxson, D.E., Wilson, J., Welch, G.E., "Comparison Between Simulated and Experimentally Measured Performance of a Four Port Wave Rotor," AIAA 2007-5049, 43rd AIAA/ASME/SAE/ASEE Joint Propulsion Conference & Exhibit, Cincinnati, OH, July 8-11, 2007.

21.) Elharis, T., Wijeyakulasuriya, S., and Nalim, M. R., "Wave Rotor Combustor Aerothermodynamic Design and Model Validation Based on Initial Testing," AIAA Paper 2010-7041, July, 2010.

22.) Paxson, D. E., "An Incidence Loss Model for Wave Rotors with Axially Aligned Passages," AIAA paper 98-3251, July, 1998.

23.) Paxson, D. E. And Wilson, J., "Recent Improvements to and Validation of the One Dimensional NASA Wave Rotor Model," NASA TM 106913, May, 1995.

24.) Paxson, D. E., "A General Numerical Model for Wave Rotor Analysis," NASA TM 105740, July,1992.

25.) Akbari, P., Müller, N., "Wave Rotor Research Program at Michigan State University," AIAA Paper 2005-3844, 41st AIAA/ASME/SAE/ASEE Joint Propulsion Conference and Exhibit, Tucson, AZ, July 10-13, 2005.

26.) Kharazi, A., Akbari, P., Müller, N., "Performance Benefits of R718 Turbo-Compression Cycle Using 3-Port Condensing Wave Rotors," IMECE2004-60992,

Proceedings of IMECE 04, 2004 ASME International Mechanical Engineering, Anaheim, CA, November 13–19, 2004.

27.) Incropera, F. P., Dewitt, D. P., Bergman, T. L., Lavine, A. S., *Fundamentals of Heat and Mass Transfer*, 6th ed., John Wiley & Sons, Hoboken, NJ, 2007, Chap. 1.

28.) Holman, J.P., *Experimental Methods for Engineers*, 3rd ed., McGraw-Hill, New York, 1978, Chap. 7.

29.) Hughes, I. G., Hase, T. P. A., *Measurements and Their Uncertainties*, 1st ed., Oxford University Press, Oxford, Great Britain, 2010, Chap. 4.

30.) Smith, B.D., Polanka, M. D., Paxson, D. E., Hoke, J. L., "Scaling Study of Wave Rotor Turbo Normalization of an Internal Combustion Engine," AIAA Paper 2012-3837, 48th AIAA/ASME/SAE/ASEE Joint Propulsion Conference and Exhibit, Atlanta, GA, July 30-August 1, 2012.

31.) Zehnder, A., Mayer, A., Matthews, L., "The Free Running Comprex$^{®}$," SAE Technical Paper 890452, International Congress and Exposition, Detroit, Michigan, Feb 27 – Mar 3, 1989.

32.) Fox, R.W., McDonald, A.T., *Introduction to Fluid Mechanics*, 3rd ed., John Wiley & Sons, Inc., New York, 1985, Chap. 8.

1. REPORT DATE *(DD-MM-YYYY)* 14-09-2012	**2. REPORT TYPE** Master's Thesis	**3. DATES COVERED** *(From – To)* August 2010 – September 2012

TITLE AND SUBTITLE Scaling Study of Wave Rotor Turbo-normalization of a Small Internal Combustion Engine	**5a. CONTRACT NUMBER**
	5b. GRANT NUMBER
	5c. PROGRAM ELEMENT NUMBER
6. AUTHOR(S) Smith, Brandon D., Lieutenant, USN	**5d. PROJECT NUMBER**
	5e. TASK NUMBER
	5f. WORK UNIT NUMBER

7. PERFORMING ORGANIZATION NAMES(S) AND ADDRESS(S) Air Force Institute of Technology Graduate School of Engineering and Management (AFIT/ENY) 2950 Hobson Way, Building 640 WPAFB OH 45433-8865	**8. PERFORMING ORGANIZATION REPORT NUMBER** AFIT/GAE/ENY/12-S48
9. SPONSORING/MONITORING AGENCY NAME(S) AND ADDRESS(ES) Air Force Research Lab, Propulsion Directorate, Turbine Combustion Branch 1790 Loop Road Wright Patterson AFB, OH 45433 Dr. Fred Schauer, (937) 656-5220; frederick.schauer@wpafb.af.mil	**10. SPONSOR/MONITOR'S ACRONYM(S)** AFRL/RQ
	11. SPONSOR/MONITOR'S REPORT NUMBER(S)

12. DISTRIBUTION/AVAILABILITY STATEMENT
APPROVED FOR PUBLIC RELEASE; DISTRIBUTION UNLIMITED.

13. SUPPLEMENTARY NOTES
This material is declared a work of the U.S. Government and is not subject to copyright protection in the United States.

14. ABSTRACT

One issue facing small Remotely Piloted Aircraft engines is their ability to maintain performance at altitude. Since many of these aircraft use commercial off the shelf engines originally designed for radio controlled aircraft and lawn care implements, the reduced pressure environment significantly degrades the operability of the engine as the altitude increases. An option to overcome this difficulty is to supercharge the system; however most superchargers are designed for larger, typically automotive, engines. As a supercharger's size is decreased, there are large efficiency losses. Therefore, there is a need to accomplish this function on a smaller scale without. One option is to utilize a device similar to the Comprex® wave rotor supercharger scaled for small engines. For this investigation, the author installed and evaluated the performance of a commercial Comprex® designed for a Mazda 626 2.0 liter diesel engine. The results were compared to simulation results from a one-dimensional computational fluid dynamics model. The loss models used by the code have been developed for and validated on wave machines designed for substantially higher corrected flow rates. Part of the current objective was to assess these scale related losses at a smaller scale. Results revealed a favorable comparison that demonstrates the loss models are applicable to the scale of the Comprex®. The computational fluid dynamics code's ability to simulate a wide range of wave rotor sizes indicated the code could be used on a pressure wave supercharger scaled to fit today's Remotely Piloted Aircraft engines to predict performance. The wave rotor code predicts the performance of the scaled pressure wave supercharger to be similar to the full sized Comprex® providing approximately two times the ambient air pressure to the engine inlet.

15. SUBJECT TERMS
Wave rotor, pressure wave supercharger, Comprex®

16. SECURITY CLASSIFICATION OF:			**17. LIMITATION OF ABSTRACT**	**18. NUMBER OF PAGES**	**19a. NAME OF RESPONSIBLE PERSON** Dr. Marc Polanka, PhD, ADVISOR
a. REPORT	**b. ABSTRACT**	**c. THIS PAGE**	UU	113	**19b. TELEPHONE NUMBER** *(Include area code)* (937) 255-6565, ext 4714
U	U	U			(marc.polanka@afit.edu)